Compromised function of an ESCRT complex promotes endolysosomal escape of tau seeds and propagation of tau aggregation

Authors:

John J. Chen[1], Diane L. Nathaniel[1], Preethi Raghavan[2], Maxine Nelson[1,3], Ruilin Tian[1,4], Eric Tse[1], Jason Y. Hong[1], Stephanie K. See[1,5], Sue-Ann Mok[1,§], Daniel R. Southworth[1,6], Lea T. Grinberg[6], Jason E. Gestwicki[1,8], Manuel D. Leonetti[2], Martin Kampmann[1,2,6,*]

Affiliations:

[1]Institute for Neurodegenerative Diseases, University of California, San Francisco, CA 94158, USA

[2]Chan Zuckerberg Biohub, San Francisco, CA 94158, USA

[3]Biomedical Sciences Graduate Program, University of California, San Francisco, CA 94158, USA

[4]Biophysics Graduate Program, University of California, San Francisco, CA 94158, USA

[5]Graduate Program in Chemistry and Chemical Biology, University of California, San Francisco, CA 94158, USA

[6]Department of Biochemistry and Biophysics, University of California, San Francisco, CA 94158, USA

[7]Department of Neurology, University of California, San Francisco, CA 94158, USA

[8]Department of Pharmaceutical Chemistry, University of California, San Francisco, CA 94158, USA

[§] Current affiliation: Department of Biochemistry, University of Alberta, Edmonton, AB, Canada, T6G 2H7

*Correspondence to: martin.kampmann@ucsf.edu

ABSTRACT

Intercellular propagation of protein aggregation is emerging as a key mechanism in the progression of several neurodegenerative diseases, including Alzheimer's Disease and frontotemporal dementia. However, we lack a systematic understanding of the cellular pathways controlling prion-like propagation. To uncover such pathways, we performed CRISPR interference (CRISPRi) screens in a human cell-based model of propagation of tau aggregation. Our screens uncovered that knockdown of components of the ESCRT-III machinery, namely CHMP6, or CHMP2A in combination with CHMP2B (a gene linked to familial frontotemporal dementia), promote propagation of tau aggregation. We found that knockdown of these genes caused damage to endolysosomal membranes, consistent with a role for the ESCRT pathway in endolysosomal membrane repair. Leakiness of the endolysosomal compartment significantly enhanced prion-like propagation of tau aggregation, likely by making tau seeds more available to pools of cytoplasmic tau. Together, these findings suggest that endolysosomal escape is a critical step in tau propagation.

INTRODUCTION

Neurodegenerative diseases are one of the most pressing challenges facing humanity. A formidable roadblock to the development of effective therapies is our incomplete understanding of the underlying molecular and cellular mechanisms. A major breakthrough was the discovery that scrapie, an infectious neurodegenerative disease, is caused by the cell-to-cell propagation of protein aggregates via "prion" forms of the protein (Prusiner, 1982). In this process, a prion seed converts healthy, native proteins to adopt an aggregated, prion conformer. More recently, findings from numerous, independent studies support the hypothesis that prion-like propagation also underlies common, non-infectious neurodegenerative diseases, such as Alzheimer's Disease (AD) (recently reviewed in (Vaquer-Alicea & Diamond, 2019)). However, the mechanisms that control aggregate uptake and propagation remain to be fully elucidated, especially in those diseases that involve cytoplasmic proteins. A systematic understanding of these mechanisms is important, both for the development of therapeutics and for furthering our understanding of why specific neuronal subtypes and brain regions are especially susceptible to specific diseases.

57 Of particular interest to us are the mechanisms controlling propagation of aggregated
58 forms of the protein tau. Tau aggregation is one of the hallmarks of AD and the levels of
59 aggregated tau correlate with cognitive deficits and neuronal loss (Gomez-Isla et al., 1997; Berg
60 et al., 1998; Giannakopoulos et al., 2003; Bejanin et al., 2017). Beyond AD, tau aggregation also
61 defines a number of other neurodegenerative diseases, collectively termed tauopathies, some of
62 which are caused by familial point mutations in tau (Wang & Mandelkow, 2016).
63 Propagation of tau aggregation can be modeled in cultured HEK293 cells that express
64 fluorescently tagged versions of tau, as first established by the Diamond lab (Frost et al., 2009).
65 In this system, addition of aggregated tau seeds to the culture media causes the fluorescently
66 tagged tau in the cells to convert from a diffuse, soluble form to aggregated puncta. This cell-
67 based model has enabled the characterization of tau species with seeding activity from patient
68 brains (Mirbaha et al., 2015), and the creation of a minimal synthetic tau that retains seeding
69 capability (Stöhr et al., 2017). Furthermore, cell-based models can also be used as a biosensor to
70 detect and propagate distinct prion strains of tau from different tauopathies (Sanders et al., 2014;
71 Kaufman et al., 2016; Woerman et al., 2016). Importantly, seeding of tau aggregation in the cell-
72 based model is predictive of *in vivo* seeding in a mouse model (Holmes et al., 2014).
73 In addition to their utility as "biosensors" for tau aggregates with prion properties, cell-
74 based models can also be used to elucidate cellular pathways that control propagation of tau
75 aggregation. Previous work from others and us leveraged cell-based models to uncover
76 mechanisms that mediate tau uptake into cells (Frost et al., 2009; Holmes et al., 2013; Rauch et
77 al., 2018; Stopschinski et al., 2018). In those studies, binding of tau to specific cell-surface
78 heparan sulfate proteoglycans was found to mediate cellular uptake. These results were validated
79 in human iPSC-derived neurons and mouse brain slices (Rauch et al., 2018), supporting the
80 physiological relevance of the cell-based model.
81 While these studies established the mechanism for tau uptake, the downstream cellular
82 pathways controlling propagation of tau aggregation have not been systematically characterized.
83 We hypothesized that tau aggregation in the cytosol would be influenced by multiple cellular
84 pathways, including those controlling trafficking of tau seeds through the endolysosomal
85 pathway, localization of tau seeds to the cytosol, templated aggregation of soluble tau, and
86 clearance of tau aggregates (**Fig. 1A**).

To uncover relevant cellular pathways downstream of tau uptake, we here combine our CRISPR interference-based genetic screening approach (Gilbert et al., 2014; Kampmann, 2018) with a cell-based model of tau aggregation using fluorescence resonance energy transfer (FRET). Using this approach, we uncover endolysosomal escape of tau seeds as a critical step in the propagation of tau aggregation. Defects in the ESCRT machinery compromise endolysosomal integrity, thereby promoting the escape of tau seeds from endolysosomal compartments and accelerating subsequent templating of tau aggregation in the cytosol. These findings provide insight into the mechanisms of tau trafficking and suggest a source for new potential therapeutic targets.

RESULTS

Cell-based model of prion-like propagation of tau aggregation

We established a cell-based model to monitor the prion-like propagation of tau aggregation in HEK293T cells. Such a model had previously been pioneered by the Diamond lab (Frost et al., 2009) and adapted for flow cytometry using a FRET-based strategy to monitor tau aggregation (Kfoury et al., 2012). In this FRET-based strategy, two versions of the tau repeat domain (RD) containing disease-associated P301L and V337M mutations are expressed as fusions with either the FRET donor CFP or the FRET acceptor YFP. When exposed to tau fibrils from recombinant or cell/brain-derived lysate sources, the CFP and YFP tags are brought into close proximity, enabling FRET. We generated a reporter line following a similar strategy (**Fig. 1B**). Instead of the CFP-YFP FRET pair, we used Clover2 and mRuby2, since proteins of this type had been shown to have a very high dynamic range for FRET, with a high Förster radius (Lam et al., 2012). We selected a monoclonal line for optimal expression and dynamic range of the FRET signal.

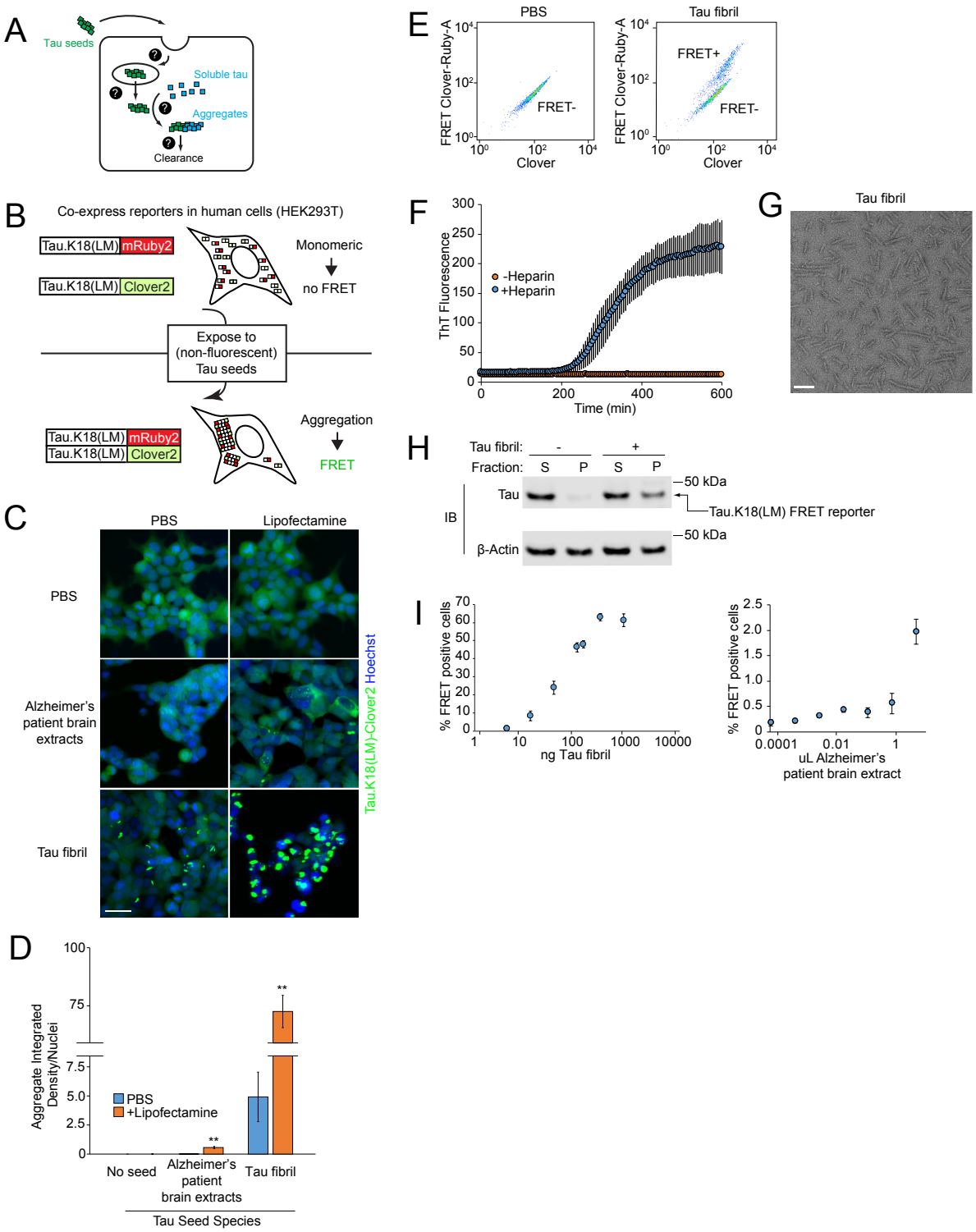

Figure 1 – legend overleaf

Figure 1 – Tau seeds induce tau aggregation in a FRET-based reporter cell line
(**A**) Overview of cellular processes that may control the prion-like tau propagation and aggregation. Question marks represent unknown cellular mechanisms. (**B**) Schematic representation of the FRET-based reporter assay to monitor tau aggregation in HEK293T cells. In the absence of tau seeds, fluorescently labeled tau.K18(LM) is monomeric. Exposure to non-fluorescent tau seeds induces aggregation of the reporter, which can be measured by the formation of tau aggregates by fluorescence microscopy or an increase in FRET intensity by flow cytometry. (**C**) Induction of fluorescent tau aggregates in FRET reporter cell line. Representative images of cells treated with PBS (top row), Alzheimer's patient brain extracts after 5 days (*second row*), or fibrils of recombinant human 0N4R tau after 2 days (*third row*). For each tau seed, each condition is complexed with (*right column*) or without (*left column*) lipofectamine. Nuclei were counter-stained with Hoechst 33342. Scale bar = 50 μm (**D**) Comparison of intracellular fluorescent tau aggregates from images in **Fig. 1C**. Integrated density quantification of fluorescent tau aggregates seeded with various tau seeds complexed with *(blue)* or without (*orange*) lipofectamine were quantified and divided by total nuclei per image. n=3 technical replicates (with at least 50 nuclei per image), error bars represent standard deviation, * $P<0.05$, ** $P<0.01$ (two-tailed Student's t test for comparison to PBS (no lipofectamine) control for each tau seeding condition). (**E**) Representative flow cytometry plot of FRET reporter cells after 2 day treatment with PBS (*left*) or tau fibrils (*right*). (**F**) Incubation of recombinant 0N4R tau with heparin and constant agitation at 37° C induces fibrillization. Fibrillization is monitored using an increase in Thioflavin T fluorescence (ex: 440 nm, em: 485 nm), which occurs in the presence (blue) of heparin (10 μg/mL), but not in the absence (orange) of heparin. Error bars represent standard deviation from n=3 technical replicates. (**G**) Representative negative stain electron micrograph of tau fibrils. Scale bar = 100 nm (**H**) Lysates from FRET reporter cells treated with PBS or tau fibrils for 2 days were fractionated at 1000xg into soluble (S) or pellet (P) fractions, and subjected to SDS-PAGE and immunoblotting using antibodies against tau and β-actin. (**I**) Quantification of % FRET positive cells using flow cytometry across concentration ranges of tau fibrils (*left*) or human Alzheimer's patient brain extracts (*right*). Error bars represent standard deviation for n=3 technical replicates.

In the absence of seeding, these cells showed diffuse intracellular fluorescence without visible aggregates when monitored by fluorescence microscopy (**Fig. 1C,D**) and they appeared as a single population when FRET levels are monitored by flow cytometry (**Fig. 1E**). In contrast, exposure of these cells to extracts from AD patient brains caused the tau reporter constructs to aggregate, as reflected by formation of fluorescent puncta (**Fig. 1C,D**). However, seeded aggregation with brain-derived tau required co-incubation with lipofectamine 2000 (here referred to as lipofectamine) to achieve modest aggregation (**Fig. 1C,D**), consistent with reports from other groups (Holmes et al., 2014; Sanders et al., 2014; Woerman et al., 2016).

Our goal was to eliminate the use of lipofectamine, because the use of a lipocationic carrier may bypass physiologically relevant uptake or trafficking pathways. Accordingly, we purified monomeric 6xHis-tagged 0N4R human tau from *E. coli* and induced fibrillization with heparin, which we monitored by an increase in thioflavin T fluorescence (**Fig. 1F)** and by negative stain electron microscopy (**Fig. 1G**). We found that treatment of our FRET reporter cells with these tau fibrils caused robust formation of aggregates, even in the absence of

158 lipofectamine. This activity was confirmed using multiple criteria, including formation of puncta
159 by fluorescence microscopy (**Fig. 1C,D**), appearance of a FRET-positive population by flow
160 cytometry (**Fig. 1E**), and biochemical characterization of tau in the insoluble fraction (**Fig. 1H**).
161 Finally, we tested the effects of increasing concentrations of tau fibrils on our FRET-based
162 reporter. We found that 6xHis-tagged fibrils robustly triggered tau aggregation in a dose-
163 dependent manner across nearly 2 orders of magnitude in concentration in the absence of
164 lipofectamine, as quantified by the percentage of FRET positive cells (**Fig. 1I**). Brain lysates also
165 produced an increase in FRET-positive cells, although the magnitude was more modest.
166 Together, these features make our FRET-based model suitable for use in a genetic screen to
167 identify cellular factors that control prion-like propagation of tau aggregation.
168

169 **Genetic screen to identify cellular factors that control prion-like propagation of tau**
170 **aggregation**

171 In order to identify cellular factors that control propagation of tau aggregation (**Fig. 1A**), we
172 conducted a CRISPR-interference (CRISPRi)-based genetic screen (**Fig. 2A**). First, we
173 transduced the reporter cell line described above with a lentiviral expression construct for a
174 catalytically inactive Cas9-BFP-KRAB (dCas9-BFP-KRAB) fusion protein. dCas9-BFP-KRAB
175 can be directed by small guide RNAs (sgRNAs) to silence a gene of interest (Gilbert et al.,
176 2013), enabling massively parallel genetic screens in mammalian cells (Gilbert et al., 2014). We
177 then transduced the cells with pooled sgRNA libraries that target protein homeostasis factors,
178 which we designed specifically for this study based on the rationale that protein homeostasis
179 factors were likely to control or modulate tau aggregation and clearance. These libraries target
180 2,949 genes encoding genes that function in autophagy, protein folding, or the ubiquitin-
181 proteasome system with at least five independent sgRNAs for each gene, plus 750 non-targeting
182 control sgRNAs. Cells transduced with these libraries were exposed to recombinant tau fibrils at
183 concentrations that would yield FRET positive cells at 50% of the maximum percentage of
184 FRET positive cells (**Fig. 1I**), thereby maximizing the dynamic range for detecting cellular
185 factors that either increase or decrease tau aggregation. FRET negative and FRET positive cell
186 populations were separated by FACS, collecting sufficient numbers of cells from each
187 population for an average 1000x representation (cells per sgRNA elements in the library).
188 Genomic DNA was isolated and the locus encoding the sgRNAs was PCR-amplified.

Frequencies for each sgRNA in each population were determined by next generation sequencing. We evaluated genes for the effect their knockdown had on the formation of tau aggregates (**Table S1**) using our previously described bioinformatics pipeline (Kampmann et al., 2013; Gilbert et al., 2014; Kampmann et al., 2014; Tian et al., 2019).

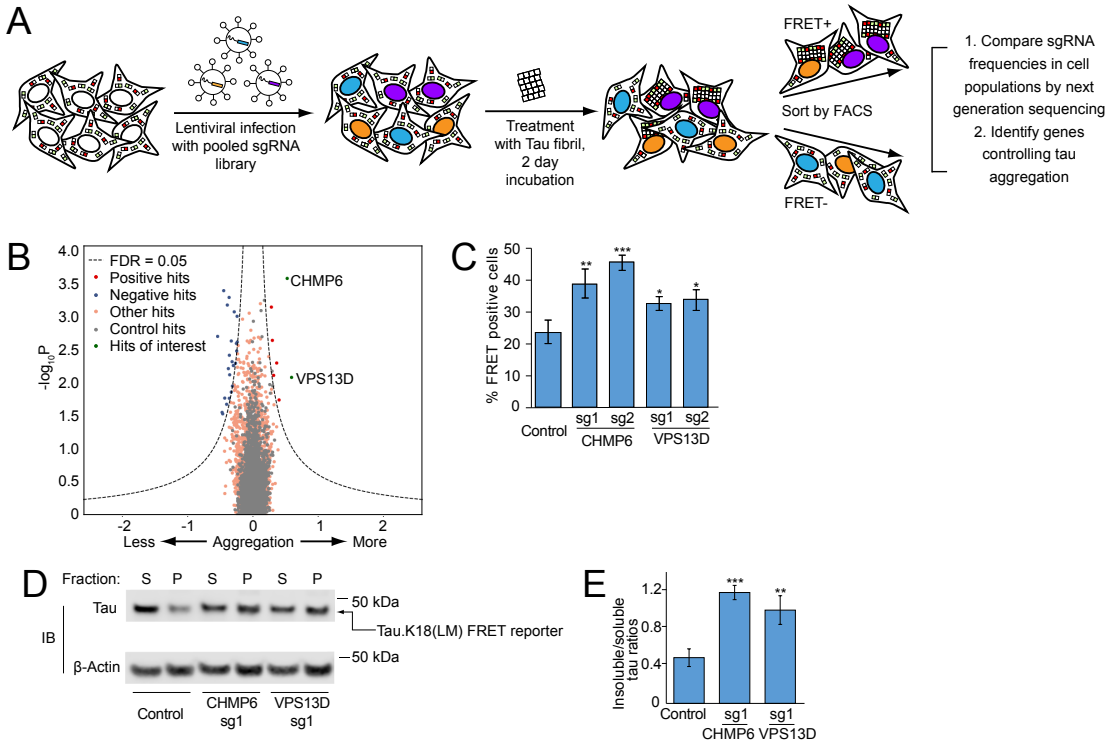

Figure 2 – CRISPRi screen for cellular factors controlling tau aggregation

(**A**) Strategy for pooled FRET-based CRISPRi screen. FRET reporter cells stably expressing the CRISPRi machinery (dCas9-BFP-KRAB) were transduced with pooled lentiviral expression libraries of sgRNAs targeting proteostasis genes. Following transduction and selection, cells were treated with tau fibrils and incubated for 2 days. Cells were detached and sorted into FRET negative and positive populations by Fluorescence-Activated Cell Sorting (FACS). sgRNA-encoding cassettes were amplified from genomic DNA of the cell populations and their frequencies were quantified using next generation sequencing to identify genes that control tau aggregation. (**B**) Volcano plot summarizing phenotypes and statistical significance (by our MAGeCK-iNC pipeline, see Materials and Methods) of the genes targeted by the sgRNA libraries. Non-targeting sgRNAs were randomly grouped into negative control "quasi-genes" (grey dots) to derive an empirical false-discovery rate (FDR). Hit genes that passed an FDR < 0.05 threshold are shown in blue (knockdown decreases aggregation) or red (knockdown increases aggregation), other genes are shown in orange. Two hit genes of interest are shown in green and labeled. (**C-E**) Validation of hit genes CHMP6 and VPS13D. FRET reporter cells transduced with individual sgRNAs targeting two hit genes or a non-targeting control sgRNA, and 5 days after transduction treated for 2 days with tau fibrils. (C) % of FRET positive cells was quantified by flow cytometry. Error bars represent standard deviation of n=3 technical replicates. *P<0.05, **P<0.01, ***P<0.001 (two-tailed Student's t test for comparison to the non-targeting control sgRNA). (D) Representative immunoblot for the tau-fluorescent protein construct in the soluble and insoluble fractions as in Fig. 1H. (E) Quantification of insoluble/soluble tau ratios from immunoblots in Fig 2D. Error bars represent standard deviation for n=3 biological replicates. P<0.05, **P<0.01, ***P<0.001 (two-tailed Student's t test for comparison to the non-targeting control sgRNA).

216

217 Two genes stood out for the strong enhancement of tau aggregation by their knockdown:
218 CHMP6 and VPS13D (**Fig. 2B**). We decided to prioritize these two genes for further
219 characterization, since both are related to genes implicated in neurodegenerative diseases.
220 CHMP6 is part of the Endosomal Sorting Complex Required for Transport (ESCRT)-III
221 complex, which is required for numerous cellular processes involving membrane remodeling
222 (Hurley, 2015). Mutations in the ESCRT-III component CHMP2B cause familial frontotemporal
223 lobar dementia (FTD) and have been shown to cause endolysosomal defects (Urwin et al., 2010;
224 Clayton et al., 2015).
225 The *VPS13* protein family is comprised of four closely-related proteins, *VPS13A-D*
226 (Velayos-Baeza et al., 2004). VPS13 family proteins are localized at various inter-organelle
227 membrane contact sites and facilitates non-vesicular lipid transport (Kumar et al., 2018; Yeshaw
228 et al., 2019). Interestingly, mutations *VPS13D* are associated with recessive ataxia (Seong et al.,
229 2018). Previously, *VPS13A* and *VPS13C* mutations have been associated with a Huntington's-
230 like syndrome (Chorea-Acanthocytosis) (Rampoldi et al., 2001; Ueno et al., 2001) and
231 Parkinson's disease (Lesage et al., 2016), respectively.
232 To confirm these screening hits, we cloned 2 individual sgRNAs each targeting CHMP6
233 and VPS13D, and confirmed target knockdown by qPCR (**Table S2**). Using these sgRNAs, we
234 validated the effect of CHMP6 and VPS13D knockdown on tau aggregation by flow cytometry
235 (**Fig. 2C**) and biochemical solubility assay (**Fig. 2D, E**).
236

237 **CHMP6 knockdown accelerates tau aggregation following tau seed uptake**

238 We next investigated the mechanism by which knockdown of CHMP6 and VPS13D might affect
239 tau aggregation. First, we excluded the possibility that knockdown of these genes alters the levels
240 of our tau reporter (**Fig. 3A**). Since we previously identified factors controlling cellular uptake of
241 tau (Rauch et al., 2018), we tested whether knockdown of CHMP6 and VPS13D impacted the
242 uptake of tau fibrils. However, we found that knockdown of the genes did not impact tau fibril
243 uptake (**Fig. 3B**), suggesting that their impact on tau aggregation is mediated downstream of seed
244 uptake.
245

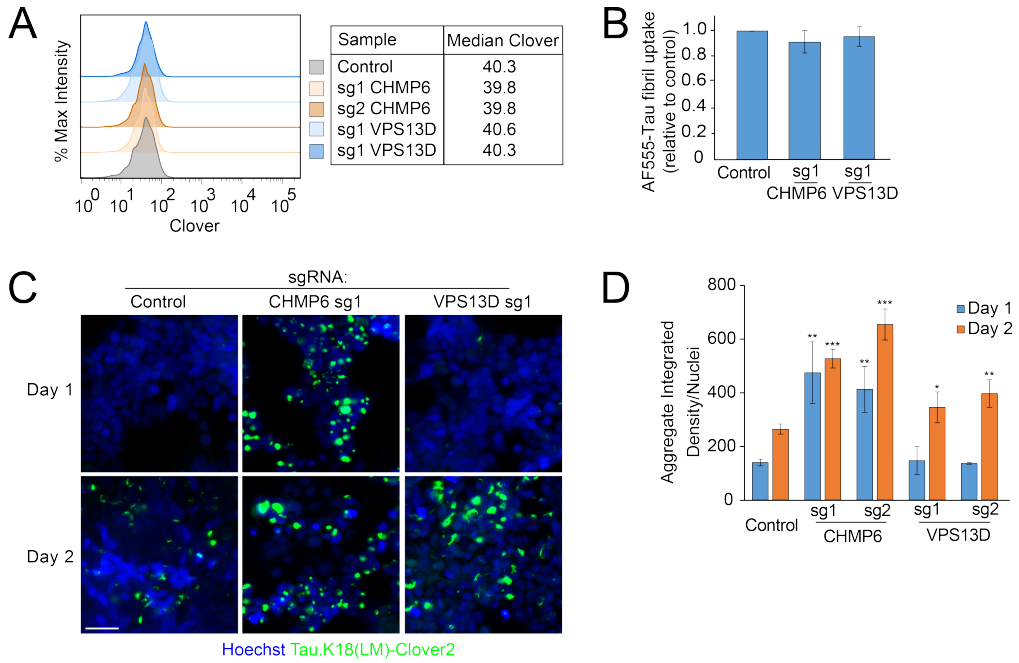

Figure 3 – CHMP6 knockdown accelerates the prion-like propagation of tau aggregation
FRET reporter cells or CRISPRi-HEK293T cells were transduced with individual sgRNAs targeting CHMP6 or VPS13D, or a non-targeting control sgRNA, and characterized for different phenotypes 5 days after transduction (**A**) Knockdown of CHMP6 and VPS13D does not impact steady state levels of the tau-Clover2 construct in FRET reporter cells, as quantified by flow cytometry. (**B**) Individual gene knockdown does not impact uptake of tau fibrils. CRISPRi HEK293T cells were incubated with AF555-labeled tau fibrils for 1 hour at 37° C, stringently washed and red fluorescence representing internalized tau fibrils was quantified by flow cytometry. Bar graph shows normalized fluorescence intensities and standard deviation of n=3 technical replicates. (**C**) CHMP6 knockdown accelerates prion-like propagation of tau aggregation. Representative fluorescence micrographs of the Tau.K18(LM)Clover2 reporter in cells 1 and 2 days after fibril addition. Nuclei were counter-stained with Hoechst 33342. Scale bar = 50 µm (**D**) Quantification of **Fig. 3C**. Tau aggregates were quantified by integrated density across the entire image and divided by total nuclei per image. Error bars represent standard deviation where n=3 images per condition (with at least 50 nuclei per image). *P<0.05, **P<0.01, ***P<0.001 (two-tailed Student's t test for comparison to the values for non-targeting control sgRNA of the same day).

We next sought to evaluate whether knockdown of CHMP6 and VPS13D increased the rate of tau aggregation, or decreased the rate of tau aggregate clearance. To this end, we utilized high-content imaging analysis to track the fibril-induced aggregation of tau over time. As expected from the results in our primary screen, we observed increased levels of aggregates 48 hours post seeding with fibrils when either CHMP6 or VPS13D were knocked down (**Fig. 3C,D**). Intriguingly, the timeline of tau aggregate formation was differentially affected by the two gene knockdowns. While VPS13D knockdown did not cause a statistically significant increase in aggregates 24 hours after treatment with tau fibrils compared to a non-targeting

271 control sgRNA, CHMP6 knockdown promoted early aggregation 24 hours post seeding (**Fig.**
272 **3C,D**). Interestingly, aggregate formation from 24 to 48 hours post-seeding did not change
273 substantially with CHMP6 knockdown, suggesting that the majority of soluble tau rapidly
274 aggregates following treatment with tau fibrils in that background. Given the intriguing
275 acceleration of tau aggregation by CHMP6, and the comparatively weaker phenotype of
276 VPS13D, we decided to focus our mechanistic studies on CHMP6.
277
278 **Endolysosomal escape of tau seeds is rate limiting for propagation of tau aggregation**
279 To investigate the mechanism by which CHMP6 knockdown accelerates seeded tau aggregation,
280 we monitored fibril entry and aggregate formation simultaneously by longitudinal imaging in
281 cells with CHMP6 knockdown compared to cells expressing a non-targeting control sgRNA.
282 (**Fig. 4A**, **Supplementary Movie 1** and **2**). In CHMP6 knockdown cells, large tau aggregates
283 rapidly formed soon after tau fibrils localized to cells, within 12 hours post seeding. In control
284 cells, by contrast, tau fibrils localized to control cells long before aggregates form. We confirmed
285 that these fibril puncta partially colocalize with the late-endosome/lysosome markers RAB7A
286 and LAMP1, and frequently localize to the lumen of RAB7A/LAMP1 positive compartments
287 (**Fig 4B, Supplementary Movie 3** and **4).** These results suggest that fibrils normally accumulate
288 in endolysosomal compartments, where they do not encounter cytosolic tau. However, CHMP6
289 knockdown seems to accelerate exit of fibrils from the endolysosomal pathway into the cytosol,
290 where it can then seed aggregation of cytosolic tau.
291 A mechanism underlying this CHMP6 phenotype is suggested by the recently reported
292 role of the ESCRT machinery in the repair of endolysosomal membrane damage (Skowyra et al.,
293 2018). We hypothesized that knocking down CHMP6 may compromise ESCRT-mediated
294 membrane repair and facilitate tau fibril escape from damaged endolysosomes. We tested this
295 hypothesis by monitoring the formation endolysosomal damage using a cytosolic GFP fusion of
296 galectin 3 (GAL3), a lectin that binds β-galactosides and forms puncta when these sugars are
297 exposed on damaged endolysosomes (Aits et al., 2015). Knocking down CHMP6 indeed caused
298 GAL3-GFP puncta, revealing endolysosomal damage (**Fig. 4C,D**). This demonstrates that
299 CHMP6 plays a critical role in the maintenance of endolysosomal integrity.
300

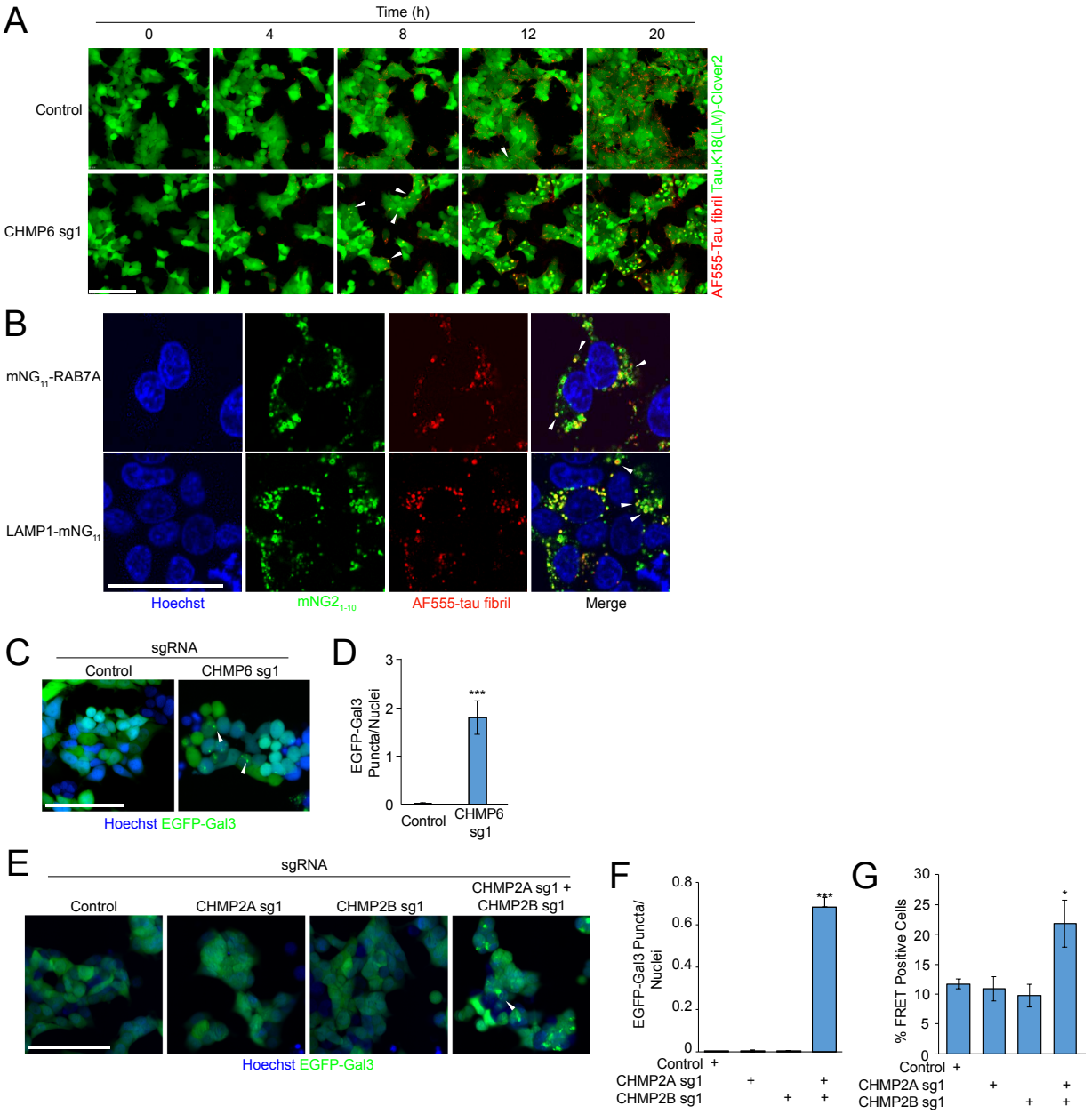

Figure 4 – CHMP6 knockdown compromises endolysosomal membrane integrity
(**A**) Time-lapse microscopy of cell entry of tau-AF555 fibrils and resulting aggregation of the cytosolic tau-Clover2 construct. Representative images of CRISPRi-HEK293T cells expressing tau.K18(LM)-clover2 transduced with either non-targeting control (top) or *CHMP6*-targeting sgRNA (bottom) are shown. Scale bar = 50 µm. Corresponding movies are provided as Supplementary Movies 1 (control sgRNA) and 2 (CHMP6 sgRNA). (**B**) Representative fluorescence microscopy images of HEK293T cells with RAB7A or LAMP1 markers endogenously labeled with the split-mNeonGreen system treated with AF555-tau fibrils for 22 hours. AF555-tau fibrils form puncta that partially co-localize with RAB7A and LAMP1-marked endocytic compartments, and in some cases localize to the inner lumen of RAB7A and LAMP1-positive compartments (white arrowheads). Scale bar = 50 µm. Corresponding movies are provided as Supplementary Movies 3 (mNG_{11}-RAB7A) or 4 (LAMP1-mNG_{11}) (**C**) CHMP6 knockdown causes endolysosomal vesicle damage. Representative fluorescence microscopy images of CRISPRi-HEK293T cells expressing an EGFP-Galectin3 (EGFP-Gal3) reporter transduced with either control (*left*)

or CHMP6 (*right*) sgRNA. Nuclei were counter-stained with Hoechst 33342. (**D**) Quantification of EGFP-Gal3 puncta divided by number of nuclei in fluorescence microscopy images shown in **Fig 4C**. Error bars represent standard deviation for n=3 technical replicates (with at least 50 nuclei per image). ***P<0.001 (two-tailed Student's t test for comparison to the non-targeting control sgRNA). (**E**) Simultaneous, but not individual, knockdown of CHMP2A and CHMP2B results in endolysosomal damage, monitored as in Fig. 4C. Nuclei were counter-stained with Hoechst 33342. Scale bar = 50 μm (**F**) Quantification of EGFP-Gal3 puncta divided by nuclei in fluorescence microscopy images shown in **Fig 4E**. Error bars represent standard deviation for n=3 technical replicates (with at least 50 nuclei per image). ***P<0.001 (two-tailed Student's t test for comparison to the non-targeting control sgRNA). (**G**) Simultaneous, but not individual, knockdown of CHMP2A and CHMP2B increases prion-like tau aggregation. % FRET positive reporter cells transduced with sgRNAs as indicated 2 days after tau fibril treatment. Error bars represent standard deviation where n=3 technical replicates. *P<0.05 (two-tailed Student's t test for comparison to the non-targeting control sgRNA).

CHMP6 was the only ESCRT protein that was a strong hit in our primary CRISPRi screen. However, other ESCRT proteins have several paralogues in the human genome, so we hypothesized that these paralogues may have been false-negatives in the CRISPRi screen because they have partially redundant functions. To test this hypothesis, we targeted CHMP2B, a gene with disease-associated mutations involved in familial frontotemporal lobar dementia (FTD). We hypothesized that its phenotype might have been masked by its close homolog, CHMP2A, which could partially compensate for a loss in CHMP2B function. Indeed, we found that simultaneous, but not individual, knockdown of CHMP2A and CHMP2B generated GAL3 puncta indicative of endolysosomal damage (**Fig. 4E,F**) and likewise promoted prion-like propagation of tau aggregation (**Fig. 4G**). This finding supports our hypothesis that maintenance of endolysosomal membrane integrity by the broader ESCRT-machinery counteracts endolysosomal escape of tau seeds.

A key implication of this model is that endolysosomal damage may promote the prion-like propagation of tau aggregation. To test this concept, we treated cells with Leucyl-Leucyl-o-Methyl-ester (LLOME), a lysosomotropic compound that accumulates in acidified organelles and rapidly forms membranolytic polymers after cleavage by cathepsin C (Thiele & Lipsky, 1990; Maejima et al., 2013; Skowyra et al., 2018). We confirmed that LLOME damages endolysosomal membranes in our cell line using the GAL3-GFP reporter (**Fig. 5A,B**). Interestingly, LLOME phenocopied CHMP6 knockdown in its acceleration of seeded tau aggregation only at concentrations where we observe endolysosomal membrane damage (**Fig. 5C**).

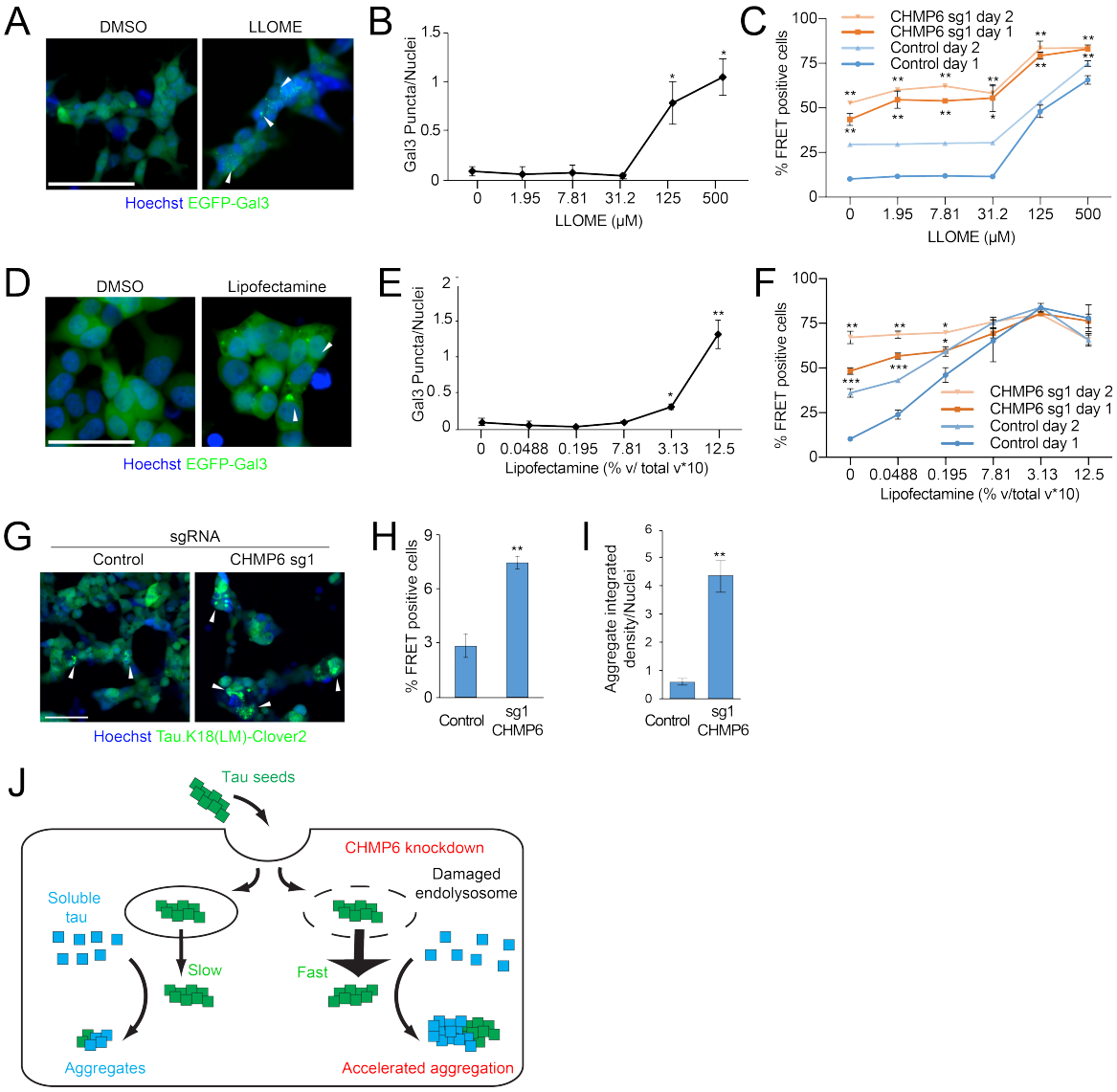

Figure 5 – Small molecules damage endolysosomal compartments and phenocopy the acceleration of the prion-like propagation of tau aggregation following CHMP6 knockdown

(**A**) Treatment with the lysosomotropic drug leucyl-leucyl-O-methyl-ester (LLOME) damages endolysosomal vesicles. Representative fluorescence microscopy images of CRISPRi-HEK293T cells expressing the EGFP-Gal3 reporter treated with DMSO (left) or 500 μM LLOME (right) for 24 h. Scale bar = 50 μm (**B**) Quantification of EGFP-Gal3 puncta divided by number of nuclei in fluorescence microscopy images shown in **Fig 5A**. Error bars represent standard deviation for n=3 technical replicates (with at least 50 nuclei per image). ***P<0.001 (two-tailed Student's t test for comparison to DMSO control). (**C**) LLOME treatment accelerates the prion-like propagation of tau aggregation. % FRET positive cells transduced with control (*blue*) or CHMP6 sgRNA (*orange*) were analyzed 24 (*dark line*) or 48 (*light line)* hours following co-treatment with DMSO or increasing concentrations of LLOME and tau fibrils. Error bars represent standard deviation for n=3 technical replicates. *P<0.05, **P<0.01 (two-tailed Student's t test for comparison to the values for non-targeting control sgRNA of the same day) (**D**) Lipofectamine treatment damages endolysosomal vesicles. Representative fluorescence microscopy images of CRISPRi-HEK293T cells expressing the EGFP-Gal3 reporter treated with DMSO (left) or 1.25 % v/v Lipofectamine 2000 (right) for 6 h. Scale bar = 50 μm (**E**) Quantification of EGFP-Gal3 puncta divided by number of nuclei in fluorescence microscopy images shown in **Fig 5D**. Error bars represent

standard deviation for n=3 technical replicates. ***P<0.001 (two-tailed Student's t test for comparison to no lipofectamine treatment). (**F**) Lipofectamine treatment accelerates the prion-like propagation of tau aggregation. % FRET positive cells transduced with control (*blue*) or CHMP6 sgRNA (*orange*) were analyzed 24 (*dark line*) or 48 (*light line)* hours following co-treatment with PBS or increasing concentrations of lipofectamine 2000 and tau fibrils. Error bars represent standard deviation where n=3 technical replicates. *P<0.05, **P<0.01, ***P<0.001 (two-tailed Student's t test for comparison to the values for non-targeting control sgRNA of the same day) (**G-I**) CHMP6 knockdown increases the prion-like propagation tau aggregation when seeding with Alzheimer's patient brain extracts. (G) Representative images of FRET reporter cells transduced with control (*left*) or CHMP6 sgRNA (*right*) and treated with Alzheimer's patient brain extract after 5 days (H) Quantification of images in **Fig. 5G**. Tau aggregates were quantified by integrated density across the entire image and divided by total nuclei per image. Error bars represent standard deviation for n=3 images per condition (with at least 50 nuclei per image). **P<0.01 (two-tailed Student's t test for comparison to non-targeting control sgRNA) (I) % FRET positive cells 5 days following treatment with Alzheimer's patient brain extract. Error bars represent standard deviation where n=3 technical replicates. **P<0.01 (two-tailed Student's t test for comparison to non-targeting control sgRNA). (**J**) Model.

As mentioned above, lipocationic reagents, such as Lipofectamine, are frequently used to deliver tau aggregates to cells for in vitro studies of prion-like propagation (Nonaka et al., 2010; Holmes et al., 2014; Woerman et al., 2016). Interestingly, these agents have previously been demonstrated to induce endolysosomal damage (Zhou & Huang, 1994). Thus, lipocationic agents might facilitate cargo delivery and escape, in part, by causing endolysosomal membrane damage. Indeed, we found that GAL3 puncta indicative of endolysosomal damage are visible 24 hours after treating cells with Lipofectamine (**Fig. 5D,E)**. Moreover, pre-treatment with lipofectamine 6 hours prior to seeding cells with tau fibrils significantly increased the formation of tau aggregates in a concentration-dependent manner, including at concentrations lower than the threshold required to induce a Gal3 reporter response (**Fig. 5F**). This suggests that lipofectamine may assist in the prion-like spread of tau aggregates both by acting as a delivery vehicle and damaging endolysosomal membranes.

When we combined CHMP6 knockdown with either LLOME or lipofectamine treatment, we found that the relative impact of CHMP6 knockdown on tau aggregate seeding was diminished in the presence of LLOME (**Fig. 5C**) or lipofectamine (**Fig. 5F**), supporting the idea that CHMP6 knockdown and LLOME/lipofectamine treatment promote propagation of tau aggregation at least partially via the same mechanism.

Finally, we wanted to validate the CHMP6 phenotype using tau seeds derived from Alzheimer's patient brain-derived extracts. Indeed, we found that CHMP6 knockdown increased the rate of tau aggregation in our reporter line seeded with patient brain-derived tau by both

407 microscopy (**Fig. 5G,H**) and flow cytometry (**Fig. 5I**). Taken together, our results support
408 endolysosomal escape of tau seeds as a rate-limiting step in our cell-based model of prion-like
409 tau propagation. Propagation can be accelerated by compromising endolysosomal integrity either
410 by directly damaging endolysosomes or by interfering with their repair through the ESCRT
411 machinery (**Fig. 5J**).
412
413
414 **DISCUSSION**
415 Using our CRISPRi-based genetic screening platform in a cell-based model of prion-like
416 propagation of tau aggregation, we found that defects in the ESCRT machinery compromise the
417 integrity of the endolysosomal pathway and thereby promote endolysosomal escape of tau seeds
418 and accelerated propagation of tau aggregation. While our observations were made in a cell-
419 based model, it is intriguing to speculate that they are relevant for propagation of tau aggregation
420 in the context of neurodegenerative diseases. Indeed, endolysosomal changes are among the first
421 cellular symptoms in Alzheimer's Disease (Cataldo et al., 2000), and have been postulated to be
422 a central driver of pathogenesis in many neurodegenerative diseases (Hu et al., 2015; Schreij et
423 al., 2016; Small et al., 2017). Furthermore, several risk genes for neurodegenerative diseases are
424 thought to function in the endolysosomal pathway, including CHMP2B (Skibinski et al., 2005).
425 While the ESCRT-III subunit CHMP6 was a top hit in our genetic screen, CHMP2B
426 knockdown by itself did not have a major impact on endolysosomal integrity and the propagation
427 of tau aggregation. This was likely the case because human cells express CHMP2A, a paralogue
428 of CHMP2B which can mostly compensate for CHMP2B in our cell-based model – combined
429 knockdown of CHMP2A and CHMP2B phenocopied CHMP6 knockdown. CHMP6 does not
430 have a paralogue in mammalian cells and is an essential gene, whereas CHMP2B is non-
431 essential, based on the Cancer dependency map, depmap.org (Tsherniak et al., 2017) , and
432 knockout mouse phenotypes (Bult et al., 2019). This provides a rationale for CHMP6 deficiency
433 not being associated with neurodegenerative diseases – it may not be compatible with life.
434 CHMP2B deficiency can be expected to cause a milder phenotype that is unmasked only later in
435 life.
436 Many mechanisms have been proposed to explain the toxicity of tau aggregates.
437 Intriguingly, tau aggregates can damage membranes in vitro (Ait-Bouziad et al., 2017), and may

damage the endolysomal pathway in patient neurons. In combination with our findings, such a mechanism of toxicity would predict a "vicious circle" or positive-feedback loop, in which tau aggregates would damage the endolysosomal pathway, thereby promoting their own propagation. They could also promote spreading of other aggregates, compatible with the co-occurrence of different protein pathologies, such as tau and a-synuclein, in many cases of neurodegenerative disease (Yan et al., 2018).

In summary, our results further support the concept that therapeutic strategies aimed at maintaining or restoring the function of the endolysosomal pathway or promoting its repair may be promising in neurodegenerative diseases. Future studies will be aimed at understanding mechanisms underlying the VPS13D phenotype, which seems distinct from the endolysosomal escape pathway controlled by CHMP6.

While our genetic screen with libraries targeting protein homeostasis factors unexpectedly uncovered the ESCRT machinery in counter-acting endolysosomal escape of tau, we had expected to find molecular chaperones or co-chaperones controlling tau aggregation among the top hits. Results obtained *in vitro* (Voss et al., 2012; Baughman et al., 2018; Kundel et al., 2018; Mok et al., 2018) and *in vivo* (Abisambra et al., 2010) suggest that specific chaperones and co-chaperones can strongly modulate tau aggregation, and are potential therapeutic targets for tauopathies (Young et al., 2018). The fact that knockdown of individual chaperones did not have a major impact on tau aggregation could be due to redundancy in the chaperone network of cells. Future CRISPR activation (CRISPRa) screens have the potential to yield complementary results by over-expressing endogenous genes (Gilbert et al., 2014; Kampmann, 2018) and may reveal relevant chaperones in the cellular context.

Finally, future screens in iPSC-derived neurons using our recently developed platform (Tian et al., 2019) may reveal additional, neuron-specific pathways, and also uncover factors that underlie selective vulnerability of specific neuronal subtypes (Kampmann, 2017).

466 **MATERIALS AND METHODS**

467

468 **Preparation of extracts from Alzheimer's Disease patient brains**

469 The Alzheimer's Disease brain sample was received from the Neurodegenerative Brain Bank of
470 the UCSF Memory and Aging Center (UCSF/MAC) . All research participants at UCSF/MAC
471 undergo longitudinal clinical and imaging assessment. Upon death, the fresh brain was slabbed
472 into 8- to 10-mm thick coronal slabs upon procurement. These slabs were alternately fixed, in 10%
473 neutral buffered formalin for 72 hours, or snap frozen. Twenty-six tissue blocks covering
474 dementia-related regions of interest were dissected from the fixed slabs, and hematoxylin and
475 eosin and immunohistochemical stains were applied following standard diagnostic procedures
476 developed for patients with dementia (Hyman & Trojanowski, 1997; Tartaglia et al., 2010).
477 Immunohistochemistry was performed using antibodies against TDP-43 (rabbit, 1:2000,
478 Proteintech Group, Chicago, IL, USA), hyperphosphorylated tau (CP-13, S202/T205, mouse,
479 1:250, courtesy of P. Davies), beta-amyloid (1-16, mouse, clone DE2, 1:500, Millipore, Billerica,
480 MA, USA), alpha-synuclein (LB509, mouse, 1:5000, courtesy of J. Trojanowski and V. Lee). All
481 immunohistochemical runs included positive control sections to exclude technical factors as a
482 cause of absent immunoreactivity. Neuropathological diagnosis followed currently accepted
483 guidelines (Hauw et al., 1994; Dickson et al., 2002; McKeith et al., 2005; Cairns et al., 2007;
484 Montine et al., 2012). For this study, a region from the parietal cortex containing high amount of
485 AD-tau pathology was sampled from a snap frozen block. A brain extract was prepared and
486 phosphotungstate-insoluble fractions were purified as previously described (Woerman et al.,
487 2016). The extract was diluted in PBS 1:40 in DPBS and flash frozen in liquid nitrogen and
488 stored at -80 ºC.

489

490 **Purification, characterization, labeling, and fibrillization of recombinant tau**

491 Human WT 0N4R-6xHis tau protein was expressed in Rosetta^{TM} 2(DE3) competent cells
492 (MilliporeSigma #71400-3) essentially as previously described (Mok et al., 2018). Briefly,
493 protein expression was induced with 200 µM IPTG for 3.5 hours at 30 ºC. Cells were lysed via a
494 microfluidizer (Microfluidics Cat# M-100EH) followed by boiling of the lysate for 20 min. The
495 clarified supernatant was subsequently dialyzed overnight into Buffer A (20 mM MES pH 6.8,
496 50 mM NaCl, 1mM EGTA, 1 mM MgCl2, 2 mM DTT, 0.1 mM PMSF) and purified by cation

497 exchange using a HiTrap Capto SP ImpRes column (GE Cat# 17546851) with elution buffer
498 (Buffer A with 1 M NaCl). Fractions containing tau as determined by Coomassie-stained SDS-
499 PAGE were dialyzed into PBS, concentrated with an Amicon Ultra-15 centrifugal 3 kDa MWCO
500 filter (Millipore Cat# UFC900324), endotoxin purified using a Pierce high capacity endotoxin
501 removal spin column (ThermoFisher Cat# 88274), filter sterilized using a Millex-GV syringe
502 filter unit (Millipore Cat# SLGV033RB), and snap frozen in PBS at -80 ºC. Aggregation was
503 induced by incubating 10 µM tau (0.43 mg/mL) with .022 mg/mL heparin (Fisher Cat# 9041-08-
504 1, lot# 177772) and shaken at 37 °C overnight in a shaker at 1200 rpm (VWR Cat#12620-942).
505 To generate fluorescently labeled tau fibrils, 0.6 µl 10 mg/mL Alexa Fluor-555
506 (ThermoFisher Cat# A37571), 180 µl of 0.43 mg/mL tau fibrils, and 19.4 µl 1M sodium
507 bicarbonate were mixed at room temperature in the dark for 1h. Labeled tau fibrils were
508 subsequently purified from unlabeled dye with using a Zeba 7k MWCO spin desalting column
509 (ThermoFisher Cat# 89882).
510 Tau fibrils were negatively stained with 0.75% uranyl formate (pH 5.5-6.0) on thin
511 amorphous carbon layered 400-mesh copper grids (Pelco Cat# 1GC400). Five µL of sample was
512 applied to the grid for 20s before taking the droplet off with Whatman paper, followed by two
513 washes with 5 µL ddH2O and three applications of 5 µL uranyl formate removed by vacuum.
514 Grids were imaged at room temperature using a Fei Tecnai 12 microscope operating at 120kV.
515 Images were acquired on a US 4000 CCD camera at 66873x resulting in a sampling of 2.21
516 Angstrom/pixel.
517
518 **Plasmid and library design and construction**
519 Plasmids for the FRET-based aggregation reporter were constructed by cloning a fusion of the
520 K18 repeat domain of tau containing the P301L/V337M mutation (Kfoury et al., 2012) in frame
521 with C-terminal Clover2 (Addgene #54711) or mRuby2 (Addgene #54768, (Lam et al., 2012),
522 gifts from Michael Davidson, into the lentiviral expression vector pMK1200 (Kampmann et al.,
523 2013), Addgene #84219) under the control of the constitutive EF1A promoter, to obtain
524 pMK1253 or pMK1254, respectively.
525 Pooled CRISPRi sgRNA libraries targeting human protein homeostasis genes were
526 designed using our next-generation algorithm (Horlbeck et al., 2016). SgRNA protospacers for
527 these libraries are listed in Table S2. Oligonucleotide pools encoding the library were

528 synthesized by Agilent, PCR amplified and cloned into our optimized lentiviral sgRNA
529 expression vector as previously described (Gilbert et al., 2014).
530 For generation of individual sgRNAs, pairs of oligonucleotides (IDT) were annealed and
531 ligated into our optimized lentiviral sgRNA expression vector. For double sgRNA expression
532 constructs, CHMP2B and CHMP2A targeting oligos were annealed and ligated into pMJ114 and
533 pMJ179, and a double-sgRNA vector was generated from these as previously described
534 (Adamson et al., 2016).
535 The fluorescent Gal3 reporter was PCR amplified from pEGFP-hGal3 (Addgene
536 #73080), a gift from Tamotsu Yoshimori) and Gibson cloned into pJC41, which uses the
537 pMK1200 backbone (described above) and replaces the EF1a promoter with a CAG promoter.
538
539 **Cell culture, cell line generation, and treatment conditions**
540 All cells were maintained in a tissue culture incubator (37 ºC, 5% CO_2) and checked regularly for
541 mycoplasma contamination. HEK293T cells were cultured in DMEM supplemented with 10%
542 fetal bovine serum (Seradigm Cat# 97068-085, Lot# 076B16), Pen/Strep (Life Cat# 15140122),
543 and L-glutamine (Life Cat# 25030081).
544 To generate the FRET reporter line, HEK293T cells were infected with lentivirus from
545 plasmids pMK1253 and pMK1254 and cells with the highest dynamic FRET signal 2 days after
546 seeding with tau fibrils were selected. To introduce CRISPRi functionality, the cells were
547 lentivirally transduced with pHR-SFFV-dCas9-BFP-KRAB (Addgene # 46911, a gift from
548 Stanley Qi & Jonathan Weissman (Gilbert et al., 2013)), mono-clonal cell lines were selected
549 and CRISPRi activity was validated as previously described (Tian et al., 2019).
550 Cellular markers were endogenously labeled using the split-mNeonGreen2 system (Feng
551 et al., 2017), following conditions described in (Leonetti et al., 2016). Briefly, synthetic guide
552 RNAs (IDT, Alt-R reagents) were first complexed in vitro with purified *S. Pyogenes* Cas9
553 protein (UC Berkeley Macrolab). Cas9/RNA complexes were then mixed with single-stranded
554 DNA oligo donors (IDT, Ultramer reagents) and nucleofected (Lonza Cat#AAF-1002B, Amaxa
555 program CM-130) into HEK cells stably expressing SFFV-mNeonGreen2_{1-10}. Fluorescent cells
556 were selected by flow cytometry (SONY biotechnology Cat# SH800S). Sequences for CRISPR
557 RNA and donors used are listed as follows:
558

Target	crRNA sequence	Donor oligonucleotide sequence
LAMP1 (C-term mNG11)	5'-GTGCACCAGGCTAGATAGTC -3'	5'-CCCAGAGAAAGGAACAGAGGCCCCTGCAGCTGCTGTGCCTGCGTGCACCAGGCTACATCATATCGGTAAAGGCCTTTTGCCACTCCTTGAAGTTGAGCTCGGTACCACTTCCTGGACCTTGAAACAAAACTTCCAATCCGCCACCGATAGTCTGGTAGCCTGCGTGACTCCTCTTCCTGCCGACGAGGTAGGCGATGAGG -3'
RAB7A (N-term mNG11)	5'-TAGTTTGAAGGATGACCTCT -3'	5'-TGTTTCCATCACACTCACAGTGATTTCTCCTTTTCCCCCTTTAGTTTGAAGGATGACCGAGCTCAACTTCAAGGAGTGGCAAAAGGCCTTTACCGATATGATGGGTGGCGGATTGGAAGTTTTGTTTCAAGGTCCAGGAAGTGGTACCTCTAGGAAGAAAGTGTTGCTGAAGGTTATCATCCTGGGAGATTCTGGGTAAG -3'

To generate CRISPRi-HEK293T cells that monitor EGFP-Gal3 damage or only generate tau.K18(LM)-Clover2 aggregates, CRISPRi-HEK293T cells were lentivirally transduced with pMK1253 and pJC41, and a polyclonal population was sorted by FACS.

Primary CRISPRi screen

For pooled screening of libraries, 7.5 million HEK293T cells were seeded into a 15 cm^2 plate with complete DMEM on day 0. On day 1, 5 µg of lentiviral plasmid packaging mix (Kampmann et al., 2014) and 5 µg of pooled sgRNA library plasmid was transfected using lipofectamine 2000 (ThermoFisher Cat# 11668019) and incubated for 2 days. On day 3, conditioned media was removed and filter sterilized using a Millex-GV syringe filter unit (Millipore Cat# SLGV033RB). Lentivirus was precipitated (Alstem Cat# VC100) according to manufacturer

571 protocols and resuspended in complete DMEM. 20 million FRET reporter cells were added to
572 lentivirus-containing media and seeded into a T175 flask. On day 4, media from the T175 was
573 replaced with DMEM complete with 2.5 μg/mL puromycin. On day 8, Cells infected with pooled
574 sgRNA libraries were trypsinized and replated into at 100 μl per well (25,000 cells/well) of
575 several 96-well plate. In addition, 0.3 μl of 0.43 μg/μL of tau fibrils were added to each well. 48
576 hours later, cells were trypsinized and sorted using an Aria II FACS cytometer into FRET
577 negative and FRET positive populations. Genomic DNA was isolated using a Macherey-Nagel
578 Blood L kit (Machery-Nagel Cat# 740954.20) and followed according to manufacturer protocols.
579 SgRNA-encoding regions were then amplified and sequenced as previously published (Gilbert et
580 al., 2014). Phenotypes and P values for each gene were calculated using our most recent
581 bioinformatics pipeline (https://kampmannlab.ucsf.edu/mageck-inc (Tian et al., 2019)). For
582 genes targeted by more than one sgRNA library, values for the more significant phenotype were
583 selected. Full results are listed in Table S1.
584
585 **Secondary assays based on microscopy and flow cytometry**
586 To monitor tau aggregation, FRET reporter cells were seeded (25,000 cells/well) into 100 μL per
587 well in a 96 well black bottom plates (Greiner Bio-One #655097) with 0.3 μL 0.43 mg/mL Tau
588 fibrils on day 1 and analyzed 24 or 48 hours after seeding. For Alzheimer's patient brain extracts,
589 1.5 μL extract, 0.375% total v/v Lipofectamine 2000 (ThermoFisher Cat# 11668019), and 7.85
590 μL OptiMEM (Thermo Cat# 31985062) were mixed and incubated at room temperature for 2
591 hours. Lipofectamine-brain extract complexes were then added to cells previously plated in 100
592 μL (10,000 cells/well) for 6 hours. Cells were analyzed 5 days after seeding. For analysis, cells
593 were stained with Hoechst 33342 (ThermoFisher Cat# 5553141) at 1 μg/mL and analyzed by
594 flow cytometry using a BD FACSCelesta or by fluorescence microscopy using an InCell 6000
595 (GE Cat# 28-9938-51). Digital images were analyzed using CellProfiler by counting the
596 integrated density of identified aggregates/nuclei and averaged between 3 images. Cells with
597 sgRNA knockdown were similarly analyzed using a comparable protocol 5 days after
598 transduction with individual sgRNA-encoding lentivirus.
599 For experiments measuring tau aggregation in the presence of inducers of endolysosmal
600 damage, FRET reporter cells were seeded (25,000 cells/well) into 100 μL per well in a 96 well
601 black bottom plate and treated with LLOME (Sigma Cat# L7393-500MG) at varying

602 concentrations with 0.3 μL 0.43 μg/μL Tau fibrils. For treatment with lipofectamine 2000, FRET
603 reporter cells were seeded (25,000 cells/well) into 100 μL per well in a 96 well black bottom
604 plate and treated with Lipofectamine 2000 at varying concentrations. Cells were then treated 0.3
605 μL 0.43 μg/μL Tau fibrils 6 hours later. 24 or 48 hours later after seeding, cells were stained with
606 Hoechst 33342 (1 μg/mL) and analyzed by flow cytometry using a BD FACSCelesta or by
607 fluorescence microscopy using an InCell 6000 GE (Cat# 28-9938-51). Digital images were
608 collected and analyzed using CellProfiler by quantifying the integrated density of identified
609 aggregates and Hoechst-stained nuclei. In cases where CellProfiler was unable to identify nuclei,
610 nuclei were counted interactively using ImageJ. Cells with sgRNA knockdown were similarly
611 analyzed using a comparable protocol 5 days after transduction with individual sgRNA-encoding
612 lentivirus.

613 To monitor tau fibril uptake, on day 0, CRISPRi-HEK293T cells previously transduced
614 for 5 days with lentivirus expressing single sgRNAs were seeded (25,000 cells/well) into 100 μL
615 per well in a 96-well plate. On day 1, cells were treated with 1 μL 0.39 μg/μL AF555-tau fibril
616 for 1 hr at 37 ºC and collected for analysis by flow cytometry. Median mRuby2 values were
617 calculated in FlowJo and averaged between 3 technical replicates.

618 To monitor tau.K18(LM)-Clover2 steady-state levels, on day 0, FRET reporter cells
619 previously transduced for 5 days with lentivirus expressing single sgRNAs were seeded (25,000
620 cells/well) into 100 μL per well in a 96-well plate. On day 1, cells collected for analysis by flow
621 cytometry. Median Clover2 values were calculated in FlowJo and averaged between 3 technical
622 replicates.

623 To monitor localization of AF555-labeled tau fibrils, HEK293T cells expressing
624 Tau.K18(LM)-Clover2 were seeded (12,500 cells/well) into 100 μL per well in a 96-well black
625 bottom plate (Greiner Bio-One #655097) on day 0 in complete DMEM. On day 1, 0.3 μL 0.39
626 μg/μL AF555-tau fibrils were added to cell culture media and placed into an InCell 6000 (GE
627 Cat# 28-9938-51) incubator. Images were taken by at 20 minute intervals between incubations.

628 To monitor co-localization of tau fibrils with RAB7A and LAMP1, fluorescently labeled
629 HEK293T cells were seeded in glass-bottom 96-well plates (Cellvis #P96-1.5P) pre-coated with
630 fibronectin (Roche Cat# 11051407001) at 25,000 cells cells/well in 150 μL complete DMEM
631 media (including 10% FBS). After incubation for 3 hours to allow for cell adhesion, cells were
632 treated with 0.11 μg of AF555-tau PFFs per well. 22 hours post-treatment, cells were counter-

633 stained with Hoechst 33342 (0.5 μg/mL, 30 min at 37 ºC) and imaged in complete DMEM
634 without phenol-red. Live-cell imaging was performed on a Dragonfly spinning-disk instrument
635 (Andor) at 37 ºC in 5% CO2 atmosphere equipped with a 63x/1.47 NA objective (Leica) and an
636 iXon Ultra 888 EMCCD camera (Andor), acquiring time-lapse datasets at 0.4Hz.
637 To monitor Gal3-EGFP puncta formation, CRISPRi-HEK293T cells expressing EGFP-
638 Gal3 were seeded into 100 μL per well (25,000 cells/well) in a 96 well black bottom plates and
639 treated with LLOME or Lipofectamine at varying concentrations. 24 hours after seeding, cells
640 were stained with Hoechst 33342 (1 μg/mL) and digital images were collected and analyzed by
641 an InCell 6000 by counting EGFP-Gal3 puncta/nuclei and averaged between 3 images. Cells
642 with sgRNA knockdown were similarly analyzed using a comparable protocol 5 days after
643 transduction with individual sgRNA-encoding lentivirus and puromycin selection of transduced
644 cells.
645
646 **Cell fractionation and immunoblot**
647 Cells were seeded into 3 mL at 250,000 cells/well in a 6-well dishes with 4.8 μl 0.43 mg/mL tau
648 fibrils, and harvested after 48 hours by washing with PBS and releasing with 0.25% trypsin.
649 Cells were resuspended with DMEM pre-warmed to 37 ºC, spun down and washed again with
650 PBS. Cells were resuspended in 20 μl PBS and lysed by flash freezing on dry ice and rapidly
651 thawed at 42 C. This step was repeated twice. The resulting lysate was spun at 1000xg and the
652 resulting supernatant was transferred to a new tube and respun to remove any carry-over
653 insoluble material. The pellet was rinsed 3x with PBS and resuspended to the corresponding
654 volume of supernatant and briefly sonicated with a tip sonicator (Sonopuls 2070) for a brief 1
655 second pulse at 10% maximum intensity. Equivalent fractions of total volume for 100 ng
656 supernatant and resuspended pellet were boiled with SDS loading buffer (50 mM Tris-Cl
657 (pH6.8), 2% (2 w/v) SDS, 0.1% (w/v) bromophenol blue) and 10 mM DTT, subjected to SDS-
658 PAGE on 4-12% Bis-Tris polyacrylamide gels (ThermoFisher Cat# NP0322BOX) and
659 transferred to nitrocellulose membranes. Primary antibodies against human tau (DAKO Cat#
660 A0024) and β-actin (Cell Signaling Cat# 3700) were used to detect proteins. Blots were then
661 incubated with secondary antibodies (Li-Cor Cat# 926-32213 and 926-68072) and imaged on the
662 Odyssey Fc Imaging system (Li-Cor Cat# 2800). Digital images were processed and analyzed
663 using Licor Image Studio™ software.

664

665 **qRT-PCR**

666 CRISPRi-HEK293T cells expressing a constitutive non-targeting or targeting sgRNA were
667 collected by centrifugation at 1000xg for 10 min, washed twice with ice cold PBS and processed
668 for qPCR using a RNA purification kit (Zymo Cat# D7011). 500 ng total RNA from each sample
669 were reverse transcribed using Superscript^{TM} III reverse transcriptase using an oligo(dT) primer
670 (Invitrogen Cat# 18080044). The resulting cDNA was diluted 5-fold using 10 mM Tris pH 8.0
671 and 0.67 μL of this dilution was used for each quantitative real-time PCR (qPCR) reaction.
672 qPCR reactions were set up using SensiMix 2x Mastermix (Bioline Cat# QT615-20) and
673 oligonucleotides targeting genes of interest (IDT) in triplicate and run on QuantStudio 6 Flex
674 (Applied Biosystems Cat# 4485694) using protocols according to the mastermix manufacturer's
675 specifications. All reactions were normalized to an internal loading control (GAPDH) and the
676 sgRNA activity is expressed as knockdown efficiency. The qPCR primer sequences are listed in
677 Table S2.

678

679

680 **AUTHOR CONTRIBUTIONS**

681 Conception and design: J.C.C., M.K.
682 Acquisition of data: J.C.C., D.T.N., P.R., M.N., E.T.
683 Analysis and interpretation of data: J.C.C., D.L.N., M.N., R.T., E.T., P.R., M.L., D.S., M.K.
684 Drafting or revising the article: J.C.C., M.K.
685 Contributing unpublished essential data or reagents: J.Y.H., S.K.S., S.M., L.T.G., J.E.G.

686

687

688 **ACKNOWLEDGEMENTS**

689 We thank Kathleen Keough and Nia Teerikorpi for contributing to preliminary studies. We thank
690 all co-authors, Adam Frost, Bryce Mendelsohn, Jay Debnath, Amanda Woerman, Kartika
691 Widjaja, Avi Samelson, Nina Dräger, Emmy Li, Poornima Ramkumar and other members of the
692 Kampmann Lab for discussions and feedback on the manuscript. We thank Eric Chow and Derek
693 Bogdanoff (UCSF Center for Advanced Technology) for support with next-generation
694 sequencing and Sarah Elmes (UCSF Laboratory for Cell Analysis, supported by NIH grant P30

CA082103) for support with FACS. For human tissue samples, we thank Lea Grinberg, William Seeley and the Neurodegenerative Disease Brain Bank at the University of California, San Francisco, which receives funding support from NIH grants P01AG019724 and P50AG023501, the Consortium for Frontotemporal Dementia Research, and the Tau Consortium.This work was supported by NIH grants: New Innovator Award DP2 GM119139 (M.K.), R01 AG062359 (M.K.), R56 AG057528 (M.K. and L.T.G.), U54 NS100717 (M.K.), S10 OD021741 (supporting electron microscopy), R01 NS059690 (J.E.G.), a Paul G. Allen Distinguished Investigator Award (M.K.), a Chan Zuckerberg Biohub Investigator Award (M.K.), a Tau Consortium Investigator Award (M.K. and J.E.G.), a QB3/Calico Longevity Postdoctoral Fellowship (J.J.C.), an Alzheimer's Association Postdoctoral Fellowship (J.J.C.), and a National Defense Science & Engineering Graduate Fellowship (S.K.S.).

REFERENCES

Abisambra, J. F., Blair, L. J., Hill, S. E., Jones, J. R., Kraft, C., Rogers, J., Koren, J., 3rd, Jinwal, U. K., Lawson, L., Johnson, A. G., Wilcock, D., O'Leary, J. C., Jansen-West, K., Muschol, M., Golde, T. E., Weeber, E. J., Banko, J., & Dickey, C. A. (2010). Phosphorylation dynamics regulate Hsp27-mediated rescue of neuronal plasticity deficits in tau transgenic mice. *J Neurosci, 30*(46), 15374-15382. doi:10.1523/JNEUROSCI.3155-10.2010

Adamson, B., Norman, T. M., Jost, M., Cho, M. Y., Nunez, J. K., Chen, Y., Villalta, J. E., Gilbert, L. A., Horlbeck, M. A., Hein, M. Y., Pak, R. A., Gray, A. N., Gross, C. A., Dixit, A., Parnas, O., Regev, A., & Weissman, J. S. (2016). A Multiplexed Single-Cell CRISPR Screening Platform Enables Systematic Dissection of the Unfolded Protein Response. *Cell, 167*(7), 1867-1882 e1821. doi:10.1016/j.cell.2016.11.048

Ait-Bouziad, N., Lv, G., Mahul-Mellier, A. L., Xiao, S., Zorludemir, G., Eliezer, D., Walz, T., & Lashuel, H. A. (2017). Discovery and characterization of stable and toxic Tau/phospholipid oligomeric complexes. *Nat Commun, 8*(1), 1678. doi:10.1038/s41467-017-01575-4

Aits, S., Kricker, J., Liu, B., Ellegaard, A. M., Hamalisto, S., Tvingsholm, S., Corcelle-Termeau, E., Hogh, S., Farkas, T., Holm Jonassen, A., Gromova, I., Mortensen, M., & Jaattela, M. (2015). Sensitive detection of lysosomal membrane permeabilization by lysosomal galectin puncta assay. *Autophagy, 11*(8), 1408-1424. doi:10.1080/15548627.2015.1063871

730 Baughman, H. E. R., Clouser, A. F., Klevit, R. E., & Nath, A. (2018). HspB1 and Hsc70
731 chaperones engage distinct tau species and have different inhibitory effects on amyloid
732 formation. *J Biol Chem, 293*(8), 2687-2700. doi:10.1074/jbc.M117.803411

733 Bejanin, A., Schonhaut, D. R., La Joie, R., Kramer, J. H., Baker, S. L., Sosa, N., Ayakta, N.,
734 Cantwell, A., Janabi, M., Lauriola, M., O'Neil, J. P., Gorno-Tempini, M. L., Miller, Z. A.,
735 Rosen, H. J., Miller, B. L., Jagust, W. J., & Rabinovici, G. D. (2017). Tau pathology and
736 neurodegeneration contribute to cognitive impairment in Alzheimer's disease. *Brain,*
737 *140*(12), 3286-3300. doi:10.1093/brain/awx243

738 Berg, L., McKeel, D. W., Jr., Miller, J. P., Storandt, M., Rubin, E. H., Morris, J. C., Baty, J.,
739 Coats, M., Norton, J., Goate, A. M., Price, J. L., Gearing, M., Mirra, S. S., & Saunders,
740 A. M. (1998). Clinicopathologic studies in cognitively healthy aging and Alzheimer's
741 disease: relation of histologic markers to dementia severity, age, sex, and apolipoprotein
742 E genotype. *Arch Neurol, 55*(3), 326-335.

743 Bult, C. J., Blake, J. A., Smith, C. L., Kadin, J. A., Richardson, J. E., & Mouse Genome
744 Database, G. (2019). Mouse Genome Database (MGD) 2019. *Nucleic Acids Res, 47*(D1),
745 D801-D806. doi:10.1093/nar/gky1056

746 Cairns, N. J., Bigio, E. H., Mackenzie, I. R., Neumann, M., Lee, V. M., Hatanpaa, K. J., White,
747 C. L., 3rd, Schneider, J. A., Grinberg, L. T., Halliday, G., Duyckaerts, C., Lowe, J. S.,
748 Holm, I. E., Tolnay, M., Okamoto, K., Yokoo, H., Murayama, S., Woulfe, J., Munoz, D.
749 G., Dickson, D. W., Ince, P. G., Trojanowski, J. Q., Mann, D. M., & Consortium for
750 Frontotemporal Lobar, D. (2007). Neuropathologic diagnostic and nosologic criteria for
751 frontotemporal lobar degeneration: consensus of the Consortium for Frontotemporal
752 Lobar Degeneration. *Acta Neuropathol, 114*(1), 5-22. doi:10.1007/s00401-007-0237-2

753 Cataldo, A. M., Peterhoff, C. M., Troncoso, J. C., Gomez-Isla, T., Hyman, B. T., & Nixon, R. A.
754 (2000). Endocytic pathway abnormalities precede amyloid beta deposition in sporadic
755 Alzheimer's disease and Down syndrome: differential effects of APOE genotype and
756 presenilin mutations. *Am J Pathol, 157*(1), 277-286.

757 Clayton, E. L., Mizielinska, S., Edgar, J. R., Nielsen, T. T., Marshall, S., Norona, F. E., Robbins,
758 M., Damirji, H., Holm, I. E., Johannsen, P., Nielsen, J. E., Asante, E. A., Collinge, J.,
759 consortium, F. R., & Isaacs, A. M. (2015). Frontotemporal dementia caused by CHMP2B
760 mutation is characterised by neuronal lysosomal storage pathology. *Acta Neuropathol,*
761 *130*(4), 511-523. doi:10.1007/s00401-015-1475-3

762 Dickson, D. W., Bergeron, C., Chin, S. S., Duyckaerts, C., Horoupian, D., Ikeda, K., Jellinger,
763 K., Lantos, P. L., Lippa, C. F., Mirra, S. S., Tabaton, M., Vonsattel, J. P., Wakabayashi,
764 K., Litvan, I., & Office of Rare Diseases of the National Institutes of, H. (2002). Office of
765 Rare Diseases neuropathologic criteria for corticobasal degeneration. *J Neuropathol Exp*
766 *Neurol, 61*(11), 935-946.

767 Feng, S., Sekine, S., Pessino, V., Li, H., Leonetti, M. D., & Huang, B. (2017). Improved split
768 fluorescent proteins for endogenous protein labeling. *Nat Commun, 8*(1), 370.
769 doi:10.1038/s41467-017-00494-8

770 Frost, B., Jacks, R. L., & Diamond, M. I. (2009). Propagation of tau misfolding from the outside
771 to the inside of a cell. *J Biol Chem, 284*(19), 12845-12852. doi:10.1074/jbc.M808759200

772 Giannakopoulos, P., Herrmann, F. R., Bussiere, T., Bouras, C., Kovari, E., Perl, D. P., Morrison,
773 J. H., Gold, G., & Hof, P. R. (2003). Tangle and neuron numbers, but not amyloid load,
774 predict cognitive status in Alzheimer's disease. *Neurology, 60*(9), 1495-1500.

775 Gilbert, L. A., Horlbeck, M. A., Adamson, B., Villalta, J. E., Chen, Y., Whitehead, E. H.,
776 Guimaraes, C., Panning, B., Ploegh, H. L., Bassik, M. C., Qi, L. S., Kampmann, M., &
777 Weissman, J. S. (2014). Genome-Scale CRISPR-Mediated Control of Gene Repression
778 and Activation. *Cell, 159*(3), 647-661. doi:10.1016/j.cell.2014.09.029

779 Gilbert, L. A., Larson, M. H., Morsut, L., Liu, Z., Brar, G. A., Torres, S. E., Stern-Ginossar, N.,
780 Brandman, O., Whitehead, E. H., Doudna, J. A., Lim, W. A., Weissman, J. S., & Qi, L. S.
781 (2013). CRISPR-mediated modular RNA-guided regulation of transcription in
782 eukaryotes. *Cell, 154*(2), 442-451. doi:10.1016/j.cell.2013.06.044

783 Gomez-Isla, T., Hollister, R., West, H., Mui, S., Growdon, J. H., Petersen, R. C., Parisi, J. E., &
784 Hyman, B. T. (1997). Neuronal loss correlates with but exceeds neurofibrillary tangles in
785 Alzheimer's disease. *Ann Neurol, 41*(1), 17-24. doi:10.1002/ana.410410106

786 Hauw, J. J., Daniel, S. E., Dickson, D., Horoupian, D. S., Jellinger, K., Lantos, P. L., McKee, A.,
787 Tabaton, M., & Litvan, I. (1994). Preliminary NINDS neuropathologic criteria for Steele-
788 Richardson-Olszewski syndrome (progressive supranuclear palsy). *Neurology, 44*(11),
789 2015-2019.

790 Holmes, B. B., DeVos, S. L., Kfoury, N., Li, M., Jacks, R., Yanamandra, K., Ouidja, M. O.,
791 Brodsky, F. M., Marasa, J., Bagchi, D. P., Kotzbauer, P. T., Miller, T. M., Papy-Garcia,
792 D., & Diamond, M. I. (2013). Heparan sulfate proteoglycans mediate internalization and
793 propagation of specific proteopathic seeds. *Proc Natl Acad Sci U S A, 110*(33), E3138-
794 3147. doi:10.1073/pnas.1301440110

795 Holmes, B. B., Furman, J. L., Mahan, T. E., Yamasaki, T. R., Mirbaha, H., Eades, W. C.,
796 Belaygorod, L., Cairns, N. J., Holtzman, D. M., & Diamond, M. I. (2014). Proteopathic
797 tau seeding predicts tauopathy in vivo. *Proc Natl Acad Sci U S A, 111*(41), E4376-4385.
798 doi:10.1073/pnas.1411649111

799 Horlbeck, M. A., Gilbert, L. A., Villalta, J. E., Adamson, B., Pak, R. A., Chen, Y., Fields, A. P.,
800 Park, C. Y., Corn, J. E., Kampmann, M., & Weissman, J. S. (2016). Compact and highly
801 active next-generation libraries for CRISPR-mediated gene repression and activation.
802 *Elife, 5*. doi:10.7554/eLife.19760

803 Hu, Y. B., Dammer, E. B., Ren, R. J., & Wang, G. (2015). The endosomal-lysosomal system:
804 from acidification and cargo sorting to neurodegeneration. *Transl Neurodegener, 4*, 18.
805 doi:10.1186/s40035-015-0041-1

806 Hurley, J. H. (2015). ESCRTs are everywhere. *EMBO J, 34*(19), 2398-2407.
807 doi:10.15252/embj.201592484

808 Hyman, B. T., & Trojanowski, J. Q. (1997). Consensus recommendations for the postmortem
809 diagnosis of Alzheimer disease from the National Institute on Aging and the Reagan
810 Institute Working Group on diagnostic criteria for the neuropathological assessment of
811 Alzheimer disease. *J Neuropathol Exp Neurol, 56*(10), 1095-1097.

812 Kampmann, M. (2017). A CRISPR Approach to Neurodegenerative Diseases. *Trends Mol Med,*
813 *23*(6), 483-485. doi:10.1016/j.molmed.2017.04.003

814 Kampmann, M. (2018). CRISPRi and CRISPRa Screens in Mammalian Cells for Precision
815 Biology and Medicine. *ACS Chem Biol, 13*(2), 406-416.
816 doi:10.1021/acschembio.7b00657

817 Kampmann, M., Bassik, M. C., & Weissman, J. S. (2013). Integrated platform for genome-wide
818 screening and construction of high-density genetic interaction maps in mammalian cells.
819 *Proc Natl Acad Sci U S A, 110*(25), E2317-2326. doi:10.1073/pnas.1307002110

820 Kampmann, M., Bassik, M. C., & Weissman, J. S. (2014). Functional genomics platform for
821 pooled screening and generation of mammalian genetic interaction maps. *Nat Protoc,*
822 *9*(8), 1825-1847. doi:10.1038/nprot.2014.103

823 Kaufman, S. K., Sanders, D. W., Thomas, T. L., Ruchinskas, A. J., Vaquer-Alicea, J., Sharma,
824 A. M., Miller, T. M., & Diamond, M. I. (2016). Tau Prion Strains Dictate Patterns of Cell
825 Pathology, Progression Rate, and Regional Vulnerability In Vivo. *Neuron, 92*(4), 796-
826 812. doi:10.1016/j.neuron.2016.09.055

827 Kfoury, N., Holmes, B. B., Jiang, H., Holtzman, D. M., & Diamond, M. I. (2012). Trans-cellular
828 propagation of Tau aggregation by fibrillar species. *J Biol Chem, 287*(23), 19440-19451.
829 doi:10.1074/jbc.M112.346072

830 Kumar, N., Leonzino, M., Hancock-Cerutti, W., Horenkamp, F. A., Li, P., Lees, J. A., Wheeler,
831 H., Reinisch, K. M., & De Camilli, P. (2018). VPS13A and VPS13C are lipid transport
832 proteins differentially localized at ER contact sites. *J Cell Biol, 217*(10), 3625-3639.
833 doi:10.1083/jcb.201807019

834 Kundel, F., De, S., Flagmeier, P., Horrocks, M. H., Kjaergaard, M., Shammas, S. L., Jackson, S.
835 E., Dobson, C. M., & Klenerman, D. (2018). Hsp70 Inhibits the Nucleation and
836 Elongation of Tau and Sequesters Tau Aggregates with High Affinity. *ACS Chem Biol,*
837 *13*(3), 636-646. doi:10.1021/acschembio.7b01039

838 Lam, A. J., St-Pierre, F., Gong, Y., Marshall, J. D., Cranfill, P. J., Baird, M. A., McKeown, M.
839 R., Wiedenmann, J., Davidson, M. W., Schnitzer, M. J., Tsien, R. Y., & Lin, M. Z.
840 (2012). Improving FRET dynamic range with bright green and red fluorescent proteins.
841 *Nat Methods, 9*(10), 1005-1012. doi:10.1038/nmeth.2171

842 Leonetti, M. D., Sekine, S., Kamiyama, D., Weissman, J. S., & Huang, B. (2016). A scalable
843 strategy for high-throughput GFP tagging of endogenous human proteins. *Proc Natl Acad*
844 *Sci U S A, 113*(25), E3501-3508. doi:10.1073/pnas.1606731113

845 Lesage, S., Drouet, V., Majounie, E., Deramecourt, V., Jacoupy, M., Nicolas, A., Cormier-
846 Dequaire, F., Hassoun, S. M., Pujol, C., Ciura, S., Erpapazoglou, Z., Usenko, T.,
847 Maurage, C. A., Sahbatou, M., Liebau, S., Ding, J., Bilgic, B., Emre, M., Erginel-
848 Unaltuna, N., Guven, G., Tison, F., Tranchant, C., Vidailhet, M., Corvol, J. C., Krack, P.,
849 Leutenegger, A. L., Nalls, M. A., Hernandez, D. G., Heutink, P., Gibbs, J. R., Hardy, J.,
850 Wood, N. W., Gasser, T., Durr, A., Deleuze, J. F., Tazir, M., Destee, A., Lohmann, E.,
851 Kabashi, E., Singleton, A., Corti, O., Brice, A., French Parkinson's Disease Genetics, S.,
852 & International Parkinson's Disease Genomics, C. (2016). Loss of VPS13C Function in
853 Autosomal-Recessive Parkinsonism Causes Mitochondrial Dysfunction and Increases
854 PINK1/Parkin-Dependent Mitophagy. *Am J Hum Genet, 98*(3), 500-513.
855 doi:10.1016/j.ajhg.2016.01.014

856 Maejima, I., Takahashi, A., Omori, H., Kimura, T., Takabatake, Y., Saitoh, T., Yamamoto, A.,
857 Hamasaki, M., Noda, T., Isaka, Y., & Yoshimori, T. (2013). Autophagy sequesters
858 damaged lysosomes to control lysosomal biogenesis and kidney injury. *EMBO J, 32*(17),
859 2336-2347. doi:10.1038/emboj.2013.171

860 McKeith, I. G., Dickson, D. W., Lowe, J., Emre, M., O'Brien, J. T., Feldman, H., Cummings, J.,
861 Duda, J. E., Lippa, C., Perry, E. K., Aarsland, D., Arai, H., Ballard, C. G., Boeve, B.,
862 Burn, D. J., Costa, D., Del Ser, T., Dubois, B., Galasko, D., Gauthier, S., Goetz, C. G.,
863 Gomez-Tortosa, E., Halliday, G., Hansen, L. A., Hardy, J., Iwatsubo, T., Kalaria, R. N.,
864 Kaufer, D., Kenny, R. A., Korczyn, A., Kosaka, K., Lee, V. M., Lees, A., Litvan, I.,
865 Londos, E., Lopez, O. L., Minoshima, S., Mizuno, Y., Molina, J. A., Mukaetova-
866 Ladinska, E. B., Pasquier, F., Perry, R. H., Schulz, J. B., Trojanowski, J. Q., Yamada, M.,
867 & Consortium on, D. L. B. (2005). Diagnosis and management of dementia with Lewy
868 bodies: third report of the DLB Consortium. *Neurology, 65*(12), 1863-1872.
869 doi:10.1212/01.wnl.0000187889.17253.b1

870 Mirbaha, H., Holmes, B. B., Sanders, D. W., Bieschke, J., & Diamond, M. I. (2015). Tau
871 Trimers Are the Minimal Propagation Unit Spontaneously Internalized to Seed
872 Intracellular Aggregation. *J Biol Chem, 290*(24), 14893-14903.
873 doi:10.1074/jbc.M115.652693

874 Mok, S. A., Condello, C., Freilich, R., Gillies, A., Arhar, T., Oroz, J., Kadavath, H., Julien, O.,
875 Assimon, V. A., Rauch, J. N., Dunyak, B. M., Lee, J., Tsai, F. T. F., Wilson, M. R.,
876 Zweckstetter, M., Dickey, C. A., & Gestwicki, J. E. (2018). Mapping interactions with
877 the chaperone network reveals factors that protect against tau aggregation. *Nat Struct Mol*
878 *Biol, 25*(5), 384-393. doi:10.1038/s41594-018-0057-1

879 Montine, T. J., Phelps, C. H., Beach, T. G., Bigio, E. H., Cairns, N. J., Dickson, D. W.,
880 Duyckaerts, C., Frosch, M. P., Masliah, E., Mirra, S. S., Nelson, P. T., Schneider, J. A.,
881 Thal, D. R., Trojanowski, J. Q., Vinters, H. V., Hyman, B. T., National Institute on, A., &
882 Alzheimer's, A. (2012). National Institute on Aging-Alzheimer's Association guidelines
883 for the neuropathologic assessment of Alzheimer's disease: a practical approach. *Acta*
884 *Neuropathol, 123*(1), 1-11. doi:10.1007/s00401-011-0910-3

885 Nonaka, T., Watanabe, S. T., Iwatsubo, T., & Hasegawa, M. (2010). Seeded aggregation and
886 toxicity of {alpha}-synuclein and tau: cellular models of neurodegenerative diseases. *J*
887 *Biol Chem, 285*(45), 34885-34898. doi:10.1074/jbc.M110.148460

888 Prusiner, S. B. (1982). Novel proteinaceous infectious particles cause scrapie. *Science,*
889 *216*(4542), 136-144.

890 Rampoldi, L., Dobson-Stone, C., Rubio, J. P., Danek, A., Chalmers, R. M., Wood, N. W.,
891 Verellen, C., Ferrer, X., Malandrini, A., Fabrizi, G. M., Brown, R., Vance, J., Pericak-
892 Vance, M., Rudolf, G., Carre, S., Alonso, E., Manfredi, M., Nemeth, A. H., & Monaco,
893 A. P. (2001). A conserved sorting-associated protein is mutant in chorea-acanthocytosis.
894 *Nat Genet, 28*(2), 119-120. doi:10.1038/88821

895 Rauch, J. N., Chen, J. J., Sorum, A. W., Miller, G. M., Sharf, T., See, S. K., Hsieh-Wilson, L. C.,
896 Kampmann, M., & Kosik, K. S. (2018). Tau Internalization is Regulated by 6-O Sulfation
897 on Heparan Sulfate Proteoglycans (HSPGs). *Sci Rep, 8*(1), 6382. doi:10.1038/s41598-
898 018-24904-z

899 Sanders, D. W., Kaufman, S. K., DeVos, S. L., Sharma, A. M., Mirbaha, H., Li, A., Barker, S. J.,
900 Foley, A. C., Thorpe, J. R., Serpell, L. C., Miller, T. M., Grinberg, L. T., Seeley, W. W.,
901 & Diamond, M. I. (2014). Distinct tau prion strains propagate in cells and mice and
902 define different tauopathies. *Neuron, 82*(6), 1271-1288.
903 doi:10.1016/j.neuron.2014.04.047

904 Schreij, A. M., Fon, E. A., & McPherson, P. S. (2016). Endocytic membrane trafficking and
905 neurodegenerative disease. *Cell Mol Life Sci, 73*(8), 1529-1545. doi:10.1007/s00018-015-
906 2105-x

907 Seong, E., Insolera, R., Dulovic, M., Kamsteeg, E. J., Trinh, J., Bruggemann, N., Sandford, E.,
908 Li, S., Ozel, A. B., Li, J. Z., Jewett, T., Kievit, A. J. A., Munchau, A., Shakkottai, V.,
909 Klein, C., Collins, C. A., Lohmann, K., van de Warrenburg, B. P., & Burmeister, M.
910 (2018). Mutations in VPS13D lead to a new recessive ataxia with spasticity and
911 mitochondrial defects. *Ann Neurol, 83*(6), 1075-1088. doi:10.1002/ana.25220

912 Skibinski, G., Parkinson, N. J., Brown, J. M., Chakrabarti, L., Lloyd, S. L., Hummerich, H.,
913 Nielsen, J. E., Hodges, J. R., Spillantini, M. G., Thusgaard, T., Brandner, S., Brun, A.,
914 Rossor, M. N., Gade, A., Johannsen, P., Sorensen, S. A., Gydesen, S., Fisher, E. M., &
915 Collinge, J. (2005). Mutations in the endosomal ESCRTIII-complex subunit CHMP2B in
916 frontotemporal dementia. *Nat Genet, 37*(8), 806-808. doi:10.1038/ng1609

917 Skowyra, M. L., Schlesinger, P. H., Naismith, T. V., & Hanson, P. I. (2018). Triggered
918 recruitment of ESCRT machinery promotes endolysosomal repair. *Science, 360*(6384).
919 doi:10.1126/science.aar5078

920 Small, S. A., Simoes-Spassov, S., Mayeux, R., & Petsko, G. A. (2017). Endosomal Traffic Jams
921 Represent a Pathogenic Hub and Therapeutic Target in Alzheimer's Disease. *Trends*
922 *Neurosci, 40*(10), 592-602. doi:10.1016/j.tins.2017.08.003

923 Stöhr, J., Wu, H., Nick, M., Wu, Y., Bhate, M., Condello, C., Johnson, N., Rodgers, J., Lemmin,
924 T., Acharya, S., Becker, J., Robinson, K., Kelly, M. J. S., Gai, F., Stubbs, G., Prusiner, S.
925 B., & DeGrado, W. F. (2017). A 31-residue peptide induces aggregation of tau's
926 microtubule-binding region in cells. *Nat Chem, 9*(9), 874-881. doi:10.1038/nchem.2754

927 Stopschinski, B. E., Holmes, B. B., Miller, G. M., Manon, V. A., Vaquer-Alicea, J., Prueitt, W.
928 L., Hsieh-Wilson, L. C., & Diamond, M. I. (2018). Specific glycosaminoglycan chain
929 length and sulfation patterns are required for cell uptake of tau versus alpha-synuclein
930 and beta-amyloid aggregates. *J Biol Chem, 293*(27), 10826-10840.
931 doi:10.1074/jbc.RA117.000378

932 Tartaglia, M. C., Sidhu, M., Laluz, V., Racine, C., Rabinovici, G. D., Creighton, K., Karydas, A.,
933 Rademakers, R., Huang, E. J., Miller, B. L., DeArmond, S. J., & Seeley, W. W. (2010).
934 Sporadic corticobasal syndrome due to FTLD-TDP. *Acta Neuropathol, 119*(3), 365-374.
935 doi:10.1007/s00401-009-0605-1

936 Thiele, D. L., & Lipsky, P. E. (1990). Mechanism of L-leucyl-L-leucine methyl ester-mediated
937 killing of cytotoxic lymphocytes: dependence on a lysosomal thiol protease, dipeptidyl
938 peptidase I, that is enriched in these cells. *Proc Natl Acad Sci U S A, 87*(1), 83-87.

939 Tian, R., Gachechiladze, M. A., Ludwig, C. H., Laurie, M. T., Hong, J. Y., Nathaniel, D.,
940 Prabhu, A. V., Fernandopulle, M. S., Patel, R., Ward, M. E., & Kampmann, M. (2019).
941 CRISPR-based platform for multimodal genetic screens in human iPSC-derived neurons.
942 *bioRxiv, 513309; doi:* https://doi.org/10.1101/513309.

943 Tsherniak, A., Vazquez, F., Montgomery, P. G., Weir, B. A., Kryukov, G., Cowley, G. S., Gill,
944 S., Harrington, W. F., Pantel, S., Krill-Burger, J. M., Meyers, R. M., Ali, L., Goodale, A.,
945 Lee, Y., Jiang, G., Hsiao, J., Gerath, W. F. J., Howell, S., Merkel, E., Ghandi, M.,
946 Garraway, L. A., Root, D. E., Golub, T. R., Boehm, J. S., & Hahn, W. C. (2017).
947 Defining a Cancer Dependency Map. *Cell, 170*(3), 564-576 e516.
948 doi:10.1016/j.cell.2017.06.010

949 Ueno, S., Maruki, Y., Nakamura, M., Tomemori, Y., Kamae, K., Tanabe, H., Yamashita, Y.,
950 Matsuda, S., Kaneko, S., & Sano, A. (2001). The gene encoding a newly discovered
951 protein, chorein, is mutated in chorea-acanthocytosis. *Nat Genet, 28*(2), 121-122.
952 doi:10.1038/88825

953 Urwin, H., Authier, A., Nielsen, J. E., Metcalf, D., Powell, C., Froud, K., Malcolm, D. S., Holm,
954 I., Johannsen, P., Brown, J., Fisher, E. M., van der Zee, J., Bruyland, M., Consortium, F.
955 R., Van Broeckhoven, C., Collinge, J., Brandner, S., Futter, C., & Isaacs, A. M. (2010).
956 Disruption of endocytic trafficking in frontotemporal dementia with CHMP2B mutations.
957 *Hum Mol Genet, 19*(11), 2228-2238. doi:10.1093/hmg/ddq100

958 Vaquer-Alicea, J., & Diamond, M. I. (2019). Propagation of Protein Aggregation in
959 Neurodegenerative Diseases. *Annu Rev Biochem*. doi:10.1146/annurev-biochem-061516-
960 045049

961 Velayos-Baeza, A., Vettori, A., Copley, R. R., Dobson-Stone, C., & Monaco, A. P. (2004).
962 Analysis of the human VPS13 gene family. *Genomics, 84*(3), 536-549.
963 doi:10.1016/j.ygeno.2004.04.012

964 Voss, K., Combs, B., Patterson, K. R., Binder, L. I., & Gamblin, T. C. (2012). Hsp70 alters tau
965 function and aggregation in an isoform specific manner. *Biochemistry, 51*(4), 888-898.
966 doi:10.1021/bi2018078

967 Wang, Y., & Mandelkow, E. (2016). Tau in physiology and pathology. *Nat Rev Neurosci, 17*(1),
968 5-21. doi:10.1038/nrn.2015.1

969 Woerman, A. L., Aoyagi, A., Patel, S., Kazmi, S. A., Lobach, I., Grinberg, L. T., McKee, A. C.,
970 Seeley, W. W., Olson, S. H., & Prusiner, S. B. (2016). Tau prions from Alzheimer's
971 disease and chronic traumatic encephalopathy patients propagate in cultured cells. *Proc*
972 *Natl Acad Sci U S A, 113*(50), E8187-E8196. doi:10.1073/pnas.1616344113

973 Yan, X., Uronen, R. L., & Huttunen, H. J. (2018). The interaction of alpha-synuclein and Tau: A
974 molecular conspiracy in neurodegeneration? *Semin Cell Dev Biol*.
975 doi:10.1016/j.semcdb.2018.05.005

976 Yeshaw, W. M., van der Zwaag, M., Pinto, F., Lahaye, L. L., Faber, A. I., Gomez-Sanchez, R.,
977 Dolga, A. M., Poland, C., Monaco, A. P., van, I. S. C., Grzeschik, N. A., Velayos-Baeza,
978 A., & Sibon, O. C. (2019). Human VPS13A is associated with multiple organelles and
979 influences mitochondrial morphology and lipid droplet motility. *Elife, 8*.
980 doi:10.7554/eLife.43561

981 Young, Z. T., Mok, S. A., & Gestwicki, J. E. (2018). Therapeutic Strategies for Restoring Tau
982 Homeostasis. *Cold Spring Harb Perspect Med, 8*(1). doi:10.1101/cshperspect.a024612

983 Zhou, X., & Huang, L. (1994). DNA transfection mediated by cationic liposomes containing
984 lipopolylysine: characterization and mechanism of action. *Biochim Biophys Acta,*
985 *1189*(2), 195-203.
986

987 **SUPPLEMENTAL TABLE AND MOVIE LEGENDS**

988

989 **Table S1 – Gene epsilon and p values for CRISPRi screens**

990 Excel spreadsheet containing the combined analyzed results for the CRISPRi screens performed
991 with the Proteostasis-focused sgRNA libraries. The counts for each library screen were analyzed
992 using our MaGecK-iNC pipeline (see materials and methods). (**Tab 1**) The columns list the gene
993 index, epsilon (phenotype, where negative valudes indicate less aggregation, positive values
994 indicate more aggregation, p-value, product (epsilon*–log10 p-value), and gene name. NTC
995 indicate "quasi-genes" composed of random sets of 5 non-targeting negative control sgRNAs.

996

997 **Table S2 – sgRNA sequences and validation**

998 (**Tabs 1-3**) List of sgRNA targets and accompanying protospacers used for CRISPRi screens.
999 The columns list the target and protospacer. (Tab 1) Endolysosome/Autophagy (Tab 2)
1000 Chaperones/Co-chaperonse (Tab 3) Ubiquitin Proteasome System. (**Tab 1,2**) Validation of target
1001 gene knockdown by CRISPRi. (Tab 4) Columns list sgRNA activity, which is expressed as
1002 percent knockdown, standard error from n=3 technical replicates, and sgRNA oligos used in
1003 experiments for single sgRNA analysis. The columns list the sgRNA, % knockdown efficiency,
1004 standard error from n=3 technical replicates, forward oligo, and reverse oligos (used for
1005 generating lentiviral sgRNA expression plasmids. (Tab 4) Oligonucleotides used for RT-qPCR
1006 analysis. The columns list the gene target, forward, and reverse primer.

1007

1008 **Supplemental Movie 1 – Time-lapse of tau aggregate formation in HEK293T cells**
1009 **expressing tau.K18(LM)-Clover2 and transduced with non-targeting control sgRNA**

1010 Time-lapse microscopy of cell entry of AF555-tau fibrils and resulting aggregation of the
1011 cytosolic tau-clover2 construct. CRISPRi-HEK293T cells expressing tau.K18(LM)-clover2
1012 transduced with a non-targeting control. Each frame represents 20 minute intervals and is played
1013 at 5 frames per second; movie starts with the addition of fibrils.

1014

1015 **Supplemental Movie 2 - Time-lapse of tau aggregate formation in HEK293T cells**
1016 **expressing tau.K18(LM)-Clover2 and transduced with CHMP6 sgRNA**

1017 Time-lapse microscopy of cell entry of AF555-tau fibrils and resulting aggregation of the
1018 cytosolic tau-clover2 construct. CRISPRi-HEK293T cells expressing tau.K18(LM)-clover2
1019 transduced with a CHMP6 sgRNA. Each frame represents 20 minute intervals and is played at 5
1020 frames per second; movie starts with the addition of fibrils.
1021
1022 **Supplemental Movie 3 – Time-lapse of AF555-tau fibrils in cells expressing tagged mNG_{11}-**
1023 **RAB7A**
1024 Time-lapse microscopy of partial co-localization of AF555-tau fibrils with RAB7A tagged
1025 vesicles. HEK293T cells with tagged mNG_{11}-RAB7A were treated with AF555-tau fibrils for 22
1026 hours before movies were acquired. Each frame represents 2.4 second intervals and is played at 5
1027 frames per second.
1028
1029 **Supplemental Movie 4 – Time-lapse of AF555-tau fibrils in cells expressing tagged mNG_{11}-**
1030 **LAMP1**
1031 Time-lapse microscopy of partial co-localization of AF555-tau fibrils with RAB7A tagged
1032 vesicles. HEK293T cells with tagged mNG_{11}-LAMP1 were treated with AF555-tau fibrils for 22
1033 hours before movies were acquired. Each frame represents 2.4 second intervals and is played at 5
1034 frames per second.